

**PRODUCTION AND CHARACTERIZATION OF
POROUS CERAMICS FOR AIRCRAFT
ARRESTING SYSTEMS**

**A Thesis Submitted to
the Graduate School of Engineering and Sciences of
İzmir Institute of Technology
in Partial Fulfillment of the Requirements for the Degree of**

MASTER OF SCIENCE

in Materials Science and Engineering

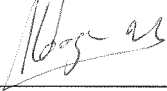
**by
Furkan ÇAPRAZ**


**July 2019
İZMİR**

We approve the thesis **Furkan ÇAPRAZ**

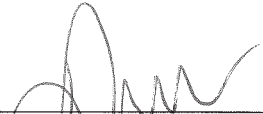
Examining Committee Members:

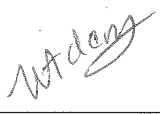

Assoc. Prof. Dr. Çekdar Vakıf AHMETOĞLU
Department of Materials Science and Engineering, İzmir Institute of Technology

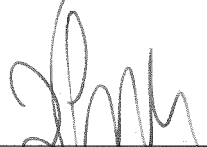

Assoc. Prof. Dr. Yaşar AKDOĞAN
Department of Materials Science and Engineering, İzmir Institute of Technology



Assoc. Prof. Dr. Mücahit SÜTÇÜ
Department of Materials Science and Engineering, İzmir Katip Çelebi University

16 July 2019


Assoc. Prof. Dr. Çekdar Vakıf AHMETOĞLU
Supervisor, Department of Materials Science and Engineering, İzmir Institute of Technology


Asst. Prof. Dr. Umut ADEM
Co-Advisor, Department of Materials Science and Engineering, İzmir Institute of Technology


Prof. Dr. Hâldun SEVİNÇLİ
Head of the Department of Materials and Engineering


Prof. Dr. Aysun SOFUOĞLU
Dean of the Graduate School of Science Engineering and Sciences

ACKNOWLEDGMENTS

I would like to thank my supervisor, Assoc. Prof. Dr. ekdar Vakıf AHMETOĐLU for his endless patience on my research. It was an honor for me to be part of his research group.

I would like to thank my family for their mentally support to me, I love you so much.

I would like to thank Ezgi OĐUR for being always with me. Also, I would like to thank TuĐe SEMERCİ, Levent KARACASULU, Ecem ÖZMEN, Öykü İÇİN, Beyza HASDEMİR, and Duygu TATLIDİL for their support and priceless friendship.

I would like to thank Center For Materials Research (CMR) and the Izmir Institute of Technology (IZTECH) for providing support to me during this thesis.

Finally, I would like to thank Esra Arıcı and my colleagues from Belenco Quartz Surfaces company.

ABSTRACT

PRODUCTION AND CHARACTERIZATION OF POROUS CERAMICS FOR AIRCRAFT ARRESTING SYSTEMS

Despite developments in aviation, accidents still occur and lead to loss of lives. Technical or environmental factors may cause overrun accidents. In the case of aircraft that fail to stop along the runway distance during take-off or landing, such accidents are called overrun. Aircraft stopping systems (AAS) are passive safety systems used to prevent to take damage of passengers and aircraft during overrun. In the literature, foamed concrete was generally used as the AAS material. However, some studies have also been carried out on other materials that may be used as the AAS material.

In present thesis, the aim was to produce porous calcium silicates instead of foamed concrete in AAS. The slip casting method was used to produce porous calcium silicate monoliths. The main components used in the manufacturing of porous wollastonite were xonotlite (as a matrix material), polymethyl methacrylate (as a sacrificial pore former, PMMA), polyvinyl alcohol (as a binder, PVA), Dolapix CE 64 (as a dispersing agent) and distilled water. Three different xonotlite ratios (8, 9 and 10% by volume) have been studied with four different xonotlite/ PMMA ratios (1, 0.82, 0.54 and 0.33 by volume). Also, specimens without PMMA were produced for each xonotlite ratio. The suspensions were stirred for 3 h at 750 rpm and then casted into the gypsum mold. The samples which were dried at room temperature (RT) were heat treated at 1000 °C. After production step microstructural, structural and mechanical analysis o the porous calcium silicates were carried out. Cold Crushing Strength (CCS) tests were performed out for determining mechanical properties. CCS values of the porous monolith parts ranged between 1376 kPa and 53.2 kPa depending on xonotlite/ PMMA ratios. In addition, the porosity values ranged from 93.38 to 87.82%. The results showed that some of these porous calcium silicate monoliths are suitable to use instead of foamed concrete as the AAS material.

ÖZET

UÇAK DURDURMA SİSTEMLERİ İÇİN GÖZENEKLİ SERAMİKLERİN ÜRETİMİ VE KARAKTERİZASYONU

Havacılıktaki gelişmelere rağmen halen uçak kazaları can kayıplarına yol açmaktadır. Pistten çıkma kazaları teknik veya çevresel faktörler nedeniyle uçağın kalkış veya iniş sırasında pist mesafesi boyunca durmaması olarak adlandırılmaktadır. Uçak Durdurma Sistemleri pistten çıkma kazalarında yolcuların ve uçağın hasar almasını engelleyen pasif güvenlik sistemleridir. Literatürde Uçak Durdurma Sistemi malzemesi olarak genellik köpürtülmüş beton kullanılmıştır. Ancak Uçak Durdurma Sistemi malzemesi olarak kullanılabilir diğer malzemeler üzerinde de bazı çalışmalar gerçekleştirilmiştir.

Bu tezde, Uçak Durdurma Sistemi malzemesi olarak köpürtülmüş beton yerine kullanılabilir gözenekli kalsiyum silikat üretimi amaçlanmıştır. Monolitik gözenekli kalsiyum silikatların üretimi için askıda döküm yöntemi kullanılmıştır. Ana malzeme olarak xonolite (temel malzeme), polimetilmetakrilat (kurban gözenek yapıcı, PMMA), polivinil alkol (bağlayıcı, PVA), Dolapix CE 64 (dağıtıcı ajan) ve su kullanılmıştır. Üç farklı xonolite oranı (hacimce %8, 9 ve 10) ile dört farklı xonolite/ PMMA oranı (hacimce 1, 0.82, 0.54 ve 0.33) üzerinde çalışılmıştır. Ayrıca tüm xonolite oranları için PMMA içermeyen numuneler üretilmiştir. Süspansiyonlar, 3 saat boyunca 750 rpm'de karıştırılmıştır ve sonra alçı kalıba dökülmüştür. Oda sıcaklığında kurutulan numunelere 1000 °C'de ısıtma işlemi uygulanmıştır. Üretim basamağından sonra mikroyapısal, yapısal ve mekanik analizler gerçekleştirilmiştir. Soğuk Kırılma Mukavemeti testi mekanik dayanımın belirlenmesi için gerçekleştirilmiştir. Gözenekli monolitlerin Soğuk Kırılma Mukavemeti, xonolite/ PMMA oranlarına bağlı olarak 1376 kPa ile 53,2 kPa arasında değişmiştir. Bunun yanında gözeneklilik değerleri % 93.38 ile 87.82 arasında değişmiştir. Sonuçlar göstermektedir ki bazı gözenekli kalsiyum silikat monolitleri Uçak Durdurma Sistemlerinde köpürtülmüş beton yerine kullanılmaya uygundur.

TABLE OF CONTENTS

LIST OF FIGURES	viii
LIST OF TABLES	x
LIST OF ABBREVIATIONS	xi
CHAPTER 1. INTRODUCTION	1
1.1. Cellular Materials	2
1.1.1 Foams	3
1.1.2 Properties of The Cellular Materials	5
1.2. Cellular Ceramics	9
1.2.1. Slip Casting	13
1.3. Cellular Calcium Silicates	16
1.4. Aircraft Arresting Systems	19
CHAPTER 2. EXPERIMENTAL PROCEDURE	23
2.1. Used Raw Materials	23
2.2. Production of Gypsum Mold	23
2.3. Production of Porous Calcium Silicates	25
2.4. Characterization	29
2.4.1. Microstructural Characterization	29
2.4.2. X-Ray Diffraction Characterization	30
2.4.3. Mechanical Characterization	30
2.4.4. Thermogravimetric Characterization	31
CHAPTER 3. EXPERIMENTAL RESULTS AND DISCUSSION	32
3.1. Raw Materials	32
3.2. Porous Monoliths	34
3.2.1. Microstructural Analysis	34
3.2.2. Structural Analysis	37
3.2.3. Mechanical Analysis	38

CHAPTER 4. CONCLUSIONS	54
REFERENCES	55

LIST OF FIGURES

<u>Figure</u>	<u>Page</u>
Figure 1.1. The number of published articles from 1993 to 2018 from Web Of Science with the topic keyword "porous materials"	1
Figure 1.2. The honeycomb (Source: Encyclopædia Britannica, 2019) and carbon nanotube structures (Source: Zhang, M and Li, J, 2009).....	2
Figure 1.3. The cellular structure of the wood (Source: Greil, P et al., 1998).....	2
Figure 1.4. Porous structure of the coffee cup (Source: Lucas, P.A., 2009)	4
Figure 1.5. Cell structure of open (Source: Yatağanababa, A. and Kurtbaşı, İ., 2016) and closed cell (Source: Bastawros, A et al., 2000)	5
Figure 1.6. The stress-strain curve of foam and showing of important regions (Source: Ashby, M.F., 2005)	6
Figure 1.7. Stress-strain diagram of the elastomeric foam (Source: Gibson , L.J and Ashby, M.F., 1999)	7
Figure 1.8. Stress-strain diagram of the plastic foam (Source: Gibson , L.J and Ashby, M.F., 1999).	8
Figure 1.9. Stress-strain diagram of the brittle foam (Source: Gibson , L.J and Ashby, M.F., 1999).	8
Figure 1.10. Produced ceramic foams for filtration of the molten metal (Source: Taslicukur, Z. et al., 2007).....	9
Figure 1.11. Schematic representation of the ceramic powder particles deposited on the mold surface during the absorption of the liquid in the slurry (Source: Rahaman, M. N., 2003)	13
Figure 1.12. SEM image of the needle shape xonotlite (Source: Black, L. et al., 2009).....	16
Figure 1.13. Schematic diagram of the CSH materials zone (Source: Shaw, S. et al., 2000).	17
Figure 1.14. Illustration of the thermal gravimetric analysis of Xonotlite and PMMA (Source: Vakifahmetoglu, C., 2014)	18
Figure 1.15. Schematic illustration of the aircraft wheel and forces formed into the EMAS (Source: Heymsfield, E. et al., 2007).....	21
Figure 1.16. The stress-strain diagram of the foamed concrete (Source: Santagata, E. et al., 2010)	21
Figure 2.1. Photographs of gypsum mold and green body of calcium silicate hydrate sample	24
Figure 2.2. Photograph of the sample which has large cracks.....	26

<u>Figure</u>	<u>Page</u>
Figure 2.3. The schematic diagram of the production procedure	28
Figure 2.4. Diagram showing heat treatment in terms of temperature and time	29
Figure 2.5. Illustration of the Cold Crushing Strength test set up	31
Figure 3.1. SEM images of the xonotlite (a) and the PMMA (b) particles	32
Figure 3.2. The particle size distribution of the PMMA particles	33
Figure 3.3. The X-Ray Diffraction pattern of the pure xonotlite powder	33
Figure 3.4. Illustration of the TGA of the xonotlite and the PMMA.....	34
Figure 3.5. The SEM images of the monolith part with no-PMMA.....	35
Figure 3.6. The SEM images of porous monoliths with decreasing xonotlite to PMMA ratio by 1, 0.82, 0.54 and 0.33, respectively	36
Figure 3.7. The SEM images of porous monoliths (A4, B4, and C4) with constant xonotlite to PMMA ratio (0.54) and increasing xonotlite content	36
Figure 3.8. The XRD patterns of xonotlite and A5 samples (a) and A (b), B (c) and C (d) series after thermal treatment	37
Figure 3.9. The compressive strength-strain diagrams of the A1 samples	38
Figure 3.10. The compressive strength-strain diagrams of the A2 samples	39
Figure 3.11. The compressive strength-strain diagrams of the A3 samples	40
Figure 3.12. The compressive strength-strain diagrams of the A4 samples	41
Figure 3.13. The compressive strength-strain diagrams of the A5 samples	42
Figure 3.14. The compressive strength-strain diagrams of the B1 samples	43
Figure 3.15. The compressive strength-strain diagrams of the B2 samples	44
Figure 3.16. The compressive strength-strain diagrams of the B3 samples	45
Figure 3.17. The compressive strength-strain diagrams of the B4 samples	46
Figure 3.18. The compressive strength-strain diagrams of the C1 samples	47
Figure 3.19. The compressive strength-strain diagrams of the C2 samples	48
Figure 3.20. The compressive strength-strain diagrams of the C3 samples	49
Figure 3.21. The compressive strength-strain diagrams of the C4 samples	50
Figure 3.22. Illustration of the compressive strength and porosity of the A series	51
Figure 3.23. Illustration of the compressive strength and porosity of the B series	52
Figure 3.24. Illustration of the compressive strength and porosity of the C series	52
Figure 3.25. Comparison of the Cold Crushing Strength of each set	53

LIST OF TABLES

<u>Table</u>	<u>Page</u>
Table 1.1. Advantages and disadvantages of Soft-Ground Arresting Systems	20
Table 2.1. Chemicals used for casting suspension in preliminary experiments.....	27
Table 2.2. Raw materials used in porous monolithic sample production	28
Table 3.1. Results of the set A1	39
Table 3.2. Results of the set A2	40
Table 3.3. Results of the set A3	41
Table 3.4. Results of the set A4	42
Table 3.5. Results of the set A5	43
Table 3.6. Results of the set B1	44
Table 3.7. Results of the set B2	45
Table 3.8. Results of the set B3	46
Table 3.9. Results of the set B4	47
Table 3.10. Results of the set C1	48
Table 3.11. Results of the set C2	49
Table 3.12. Results of the set C3	50
Table 3.13. Results of the set C4	51

LIST OF ABBREVIATIONS

AAS	Aircraft Arresting Material
CSH	Calcium Silicate Hydrates
CCS	Cold Crushing Strength
ESCO	Engineered Arresting System Corporation
EMAS	Engineered Material Arresting System
FAA	Federal Aviation Administration
PMMA	Polymethylmetacrylate
PVA	Polyvinylalcohol
RSA	Runway Safety Area
RT	Room Temperature
SEM	Scanning Electron Microscope
TGA	Thermogravimetric Analysis
XRD	X-Ray Diffraction

CHAPTER 1

INTRODUCTION

The human being has always been interested in his environment. It is also known that nature inspires humanity on many issues. The radar systems, one of the most well-known examples, are inspired by bats, and reptiles such as snakes and crocodiles inspired the camouflage used by soldiers.² The number of inventions that have been realized in the recent period has increased significantly thanks to the curiosity, analysis, and interpretation of the human species. Porous materials are one of the material types inspired by nature. For instance, human beings have used wood and bone for centuries as building material and weapon, respectively. In the literature on "porous materials," according to **Figure 1.1**, there is an enormous increase in publication number.

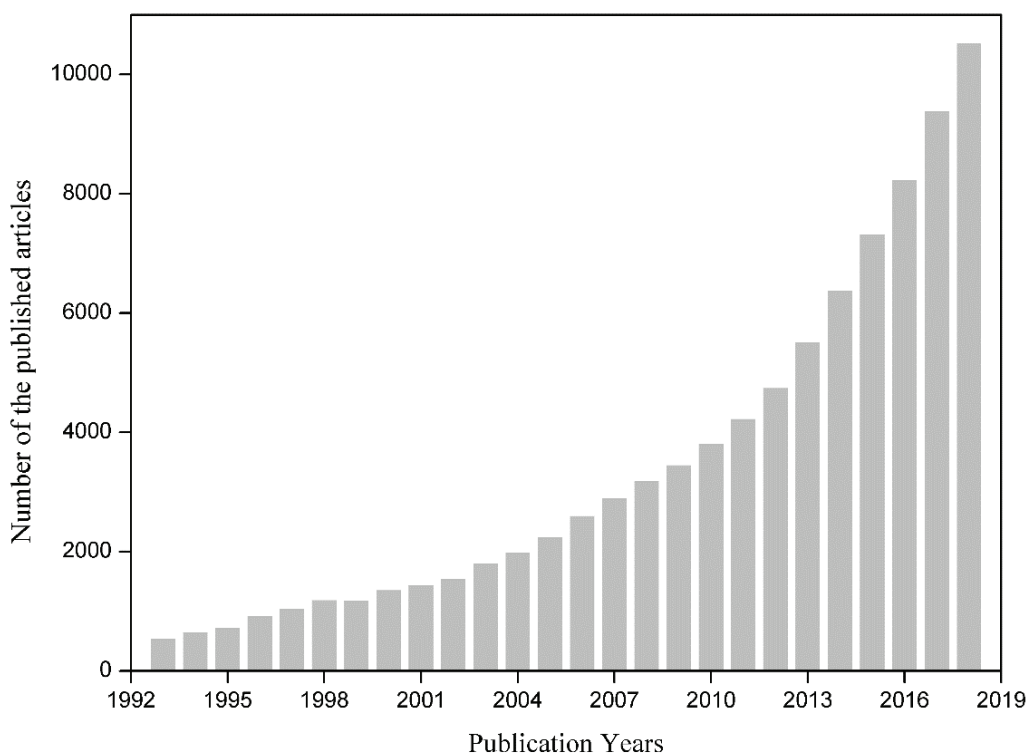


Figure 1.1. The number of published articles from 1993 to 2018 from Web Of Science with the topic keyword "porous materials".

1.1. Cellular Materials

Cellular materials can be defined as materials with spaces in many shapes (such as channels and voids) and sizes.³ On the other hand, cellular materials are contains continuously repeating lattice structures and spaces. One of the most interesting examples of cellular materials is honeycombs (see **Figure 1.2**). Because of their laminated structure (their height is shorter than their width and length), honeycombs are two-dimensional cellular materials and the cell structures are repeated in two dimensions on a regular basis.⁴ The best example for the artificial honeycomb structure as one layer is graphene. Graphene is material formed by combining carbon atoms in hexagonal order.⁵

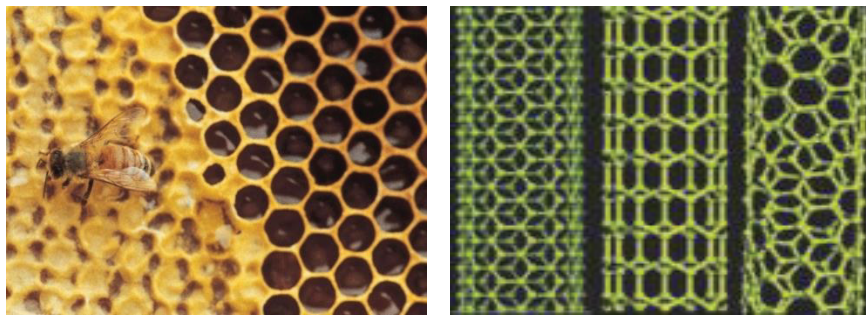


Figure 1.2. The honeycomb (Source: Encyclopædia Britannica, 2019)¹ and carbon nanotube structures (Source: Zhang, M and Li, J, 2009).⁵

Another example of cellular materials found in nature is wood. Channels (see **Figure 1.3**) with different dimensions in the structure of the trees provide relatively high strength and durability.⁶

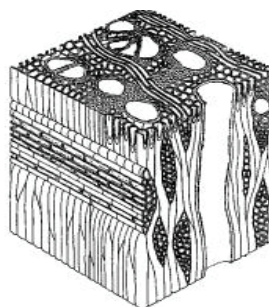


Figure 1.3. The cellular structure of the wood (Source: Greil, P et al., 1998).⁶

1.1.1. Foams

Foams are three-dimensional cellular materials.⁴ The difference between the foam and honeycomb is that cells of the foams may be arbitrarily distributed.⁷ In this thesis, the properties of foam as cellular material will be discussed. Therefore, the terms of the cellular material and the foam can be used interchangeably.

Many foam production methods in the literature have been applied and investigated for different types of materials.⁸⁻⁹ It is possible to produce many materials as cellular but there are some features that should be determined according to the application.⁴ The main uses of foams are as follows: thermal insulators, packaging/cushioning, filters and building materials. Thermal insulation materials have the highest share among the usage areas. Some of these usage areas are building walls in the construction industry or beverage cup walls in polymeric cups (see **Figure 1.4**). The thermal insulation materials used in building walls are generally polymeric foams, while the main material of the foam used in the casting pots is ceramic. Materials used in engineering applications should be designed considering the multiple parameters. Temperature, humidity and pH levels of the environment where the material is used, may be different from the normal conditions. While lightweight is desired in building applications, on the other hand, chemical inertness and thermal stability are desired in casting applications.

There are some factors that determine the mechanical, thermal and electrical characteristics of cellular materials, these factors are relative density, the structure of cells (open or closed cells, cell sizes, cell shape, pore distribution) and the properties of the material used (density, young modulus, thermal conductivity, electrical conductivity, toughness, etc.).^{4, 10} Except for the properties of the material forming the skeleton (strut) of the foam, other features can be controlled by the production method.⁸ The amount of space contained in the foams can be determined mainly by the relative density calculation. The relative density (see **Equation 1.1**) is one of the most important features of cellular materials, and this property can be calculated from the ratio of the geometric density of the foam (ρ^*) to the density (ρ_s) of the material from which the foam is made. The relative density (see **Equation 1.1**) is one of the most important features of cellular materials, and this property can be calculated from the ratio of the

geometric density of the foam (ρ^*) to the density (ρ_s) of the material from which the foam is made.

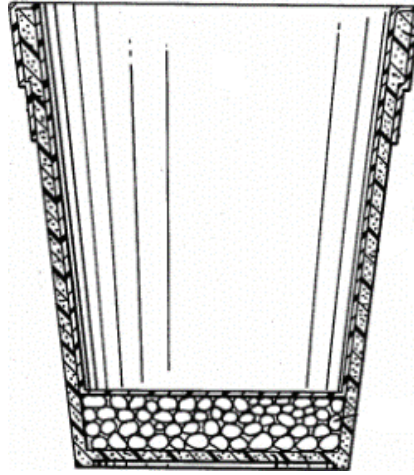


Figure 1.4. Porous structure of the coffee cup (Source: Lucas, P.A., 2009).¹¹

In general, the relative density of foam is less than the value of 0.3⁴. Above this value the material is called porous material.

$$\rho_r = \rho^* / \rho_s \quad (1.1)$$

The porosity of the foam (see **Equation 1.2**) is related to the relative density. Porosity indicates the amount of voids in the foam and can be calculated by the following formula.⁴

$$\% \Phi = (1 - \rho_r) \times 100 \quad (1.2)$$

Another feature that is as important as relative density is if the cells in the foam are open or closed. The fact that the cell structure is open means that the cell is composed only of cell corners and edges (see **Figure 1.5**). Instead, closed cell structures have cell corners, cell edges, and cell surfaces (see **Figure 1.5**).

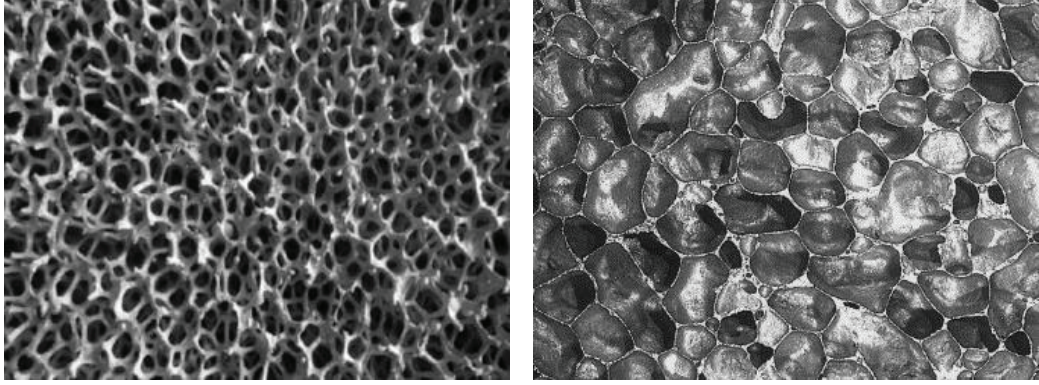


Figure 1.5. Cell structure of open (Source: Yatağanababa, A. and Kurtbaş, İ., 2016)¹² and closed cell (Source: Bastawros, A et al., 2000)¹³ aluminium foam.

1.1.2. Properties Of The Cellular Materials

Depending on the type of material, thermal conduction can be provided by free electrons (i.e. metals), lattice vibrations (i.e. ceramics) or by the movement and vibration of molecular chains (i.e. polymers).¹⁴ Considering the closed cells, the thermal conductivity of the pore filling material in the cell is generally lower than the thermal conductivity of the material constituting the cell structure, for instance, the thermal conductivity of dry air is 0.025 W/m.K but diamond has 2000 W/m.K.¹⁴ Therefore, the thermal conductivity of the foam is lower than the dense state of the same material due to the liquid resists thermal conduction flow.⁴

On the other hand, the thermal shock resistance of the foam is higher than the dense state of the same material. This attitude explained as follows: the amount of solid in the foam decreases as the amount of the void increases and the elastic modulus value decreases accordingly. Thermal shock resistance can be calculated with **Equation 1.3**¹⁴ given below, the thermal shock resistance increases while the elastic modulus decreases.^{4, 14} In particular, ceramic foams are preferred due to their high melting point and chemical inertness, as well as the high thermal shock resistance.¹⁵

$$R = \frac{\sigma_f \cdot k \cdot (1 - \nu)}{E \cdot \alpha} \quad (1.3)$$

The electrical properties of the foams vary depending on the material which are produced. In foams made of conductive material, the main structure of the foam conducts electricity, however, since the electrical conductivity is provided by free electrons and the voids in the cell prevent the movement of the free electrons, the electrical conductivity of the foam is lower than the electrical conductivity of the dense of the same material. On the other hand, if the foam is insulator material which includes high volume space and moisture may accumulate in the cavities. In this case, the electrical conductivity of the insulator material will increase due to the electrical conduction of water.

The mechanical strength of the foam, whether used for mechanical strength or for any other purpose, must be at least enough for bearing its own weight.⁴ When the stress-strain diagram of brittle foams considered, three regions are noteworthy (see **Figure 1.6**). These are elastic deformation, collapse plateau, and densification zones. Firstly, a linear elastic zone forms when the load is applied to the foam. This region is seen as a result of bending (open cell foams) or stretching (closed cell foams) of the cell walls. The slope of the graph in the linear elastic region gives the elastic modulus of the foam. If the foam is mostly composed of open cells, it means that the pressure is carried by the edges of the cells. Furthermore, as the relative density of the foam increases, the cell walls (i.e. closed cell foam) is formed and the load is partially carried by the cell edges and walls.

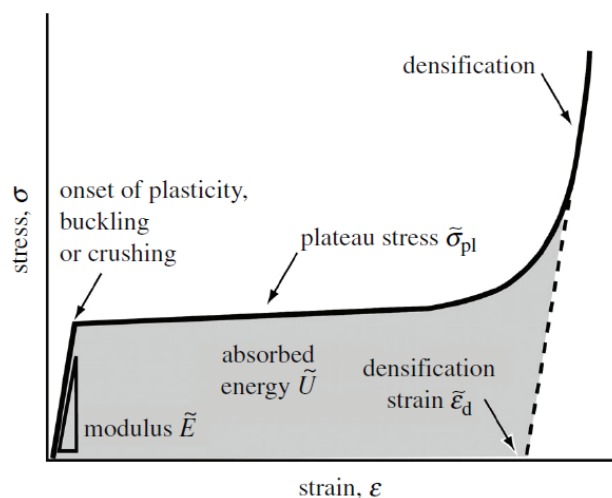


Figure 1.6. The stress-strain curve of foam and showing of important regions (Source: Ashby, M.F., 2005).¹⁶

Whatever the material characteristic behavior is, the elastic strain forms a small part of the total strain. The second region is called the collapse plateau region. This is the section where the cell walls are bent (elastomeric foams), rotates (plastic foams) or ruptures (brittle foams). In the collapse plateau region, energy absorption is achieved due to the flexing, rotating or breaking behavior of the cell walls. The collapse of the entire cell structure means that the cell edges touch the adjacent edges and volume of the cavity in the cell diminishes. Such issues are called densification, in the last region, densification is forming and the volume of space in the foam approaches to zero.^{4,9,17}

The response of the foam to bending dominated foam compressing behavior can also be classified depending on the elastic, plastic or brittle behavior of the material. When a load is applied to elastomeric foam elastic deformation occurs. The walls of the open-cell elastomeric foams are bent and the walls of the closed cell elastomeric foams are stretched. Then the cell edges are buckle after the elastic strain value has been exceeded. In the closed-cell elastomeric foams, when the edges and walls of the material collapse, the gas or liquid inside the cell compresses. This causes a force from the inside to the outside (in the opposite direction of the applied load) and provides the collapse stress to reach higher values (see **Figure 1.7**).⁴ The elastic region of the elastomeric and plastic foams is similar.⁴ In the foams which exhibit plastic behavior, in the compressive stress-strain diagram, a certain yield point is seen during the transition from the elastic region to the collapse plateau.⁹

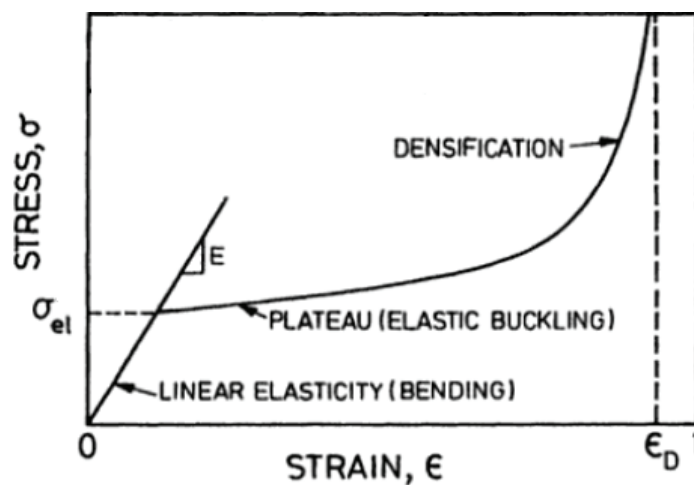


Figure 1.7. Stress-strain diagram of the elastomeric foam (Source: Gibson , L.J and Ashby, M.F., 1999).⁴

The collapse plateau and densification sections found in the compression stress-strain diagram of plastic foams are similar to the behavior of elastic foams (see **Figure 1.8**). But in the plastic foams, cell edges are hinged.⁴ Brittle foams show different behavior compared to the other two foams after the linear elastic region.

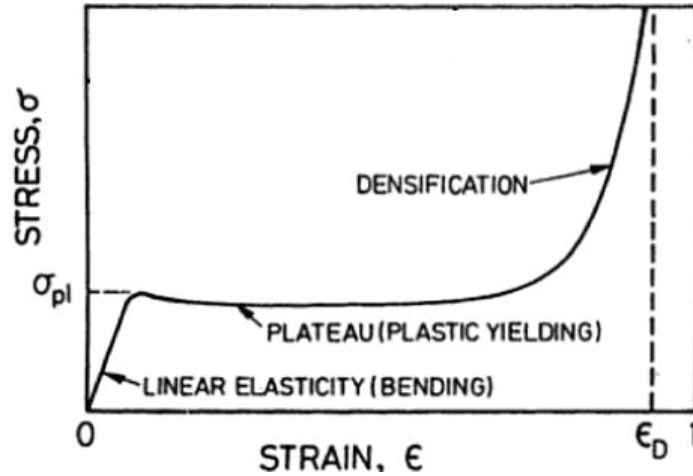


Figure 1.8. Stress-strain diagram of the plastic foam (Source: Gibson , L.J and Ashby, M.F., 1999).⁴

Under the applied load, the edges and/or walls of the cell are broken and in the stress-strain curve, after the elastic region peaks are formed (**Figure 1.9**).⁴

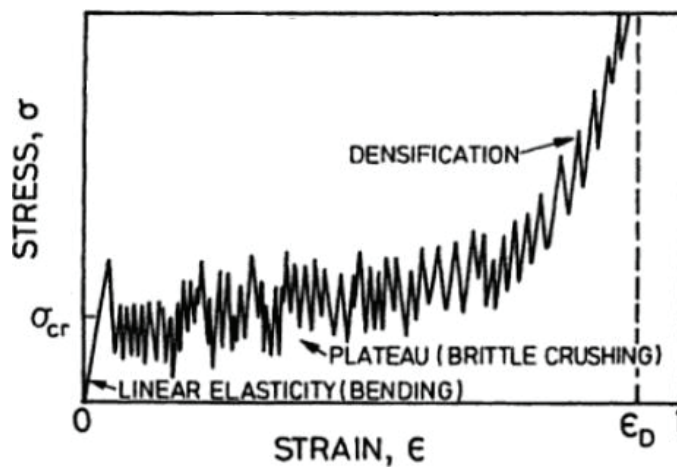


Figure 1.9. Stress-strain diagram of the brittle foam (Source: Gibson , L.J and Ashby, M.F., 1999).⁴

The tensile behavior of the foams is similar to the linear region of the compressive stress-strain curves. The part of the tensile behavior that is different from the compression behavior is collapse plateau region. Elastomeric foams are extending with stress, which increases the strain and stiffness of the material. In plastic foams, the strain occurs after the yielding point, but the strain value is low and the foam breaks after a while. In the case of brittle foams, the applied stress leads to the crack propagation and to the breakage on the weak cell walls. The strain almost never occurs.⁴

1.2. Cellular Ceramics

Cellular ceramics are highly porous materials.¹⁸⁻¹⁹ The main reason for the use of porous ceramics in many applications (such as thermal insulation, filtration of melted metals, construction materials, biomedical materials) that they have specific properties (high chemical inertness, high specific strength, high thermal shock resistance, high permeability, low thermal conductivity, low thermal mass, etc.) on a wide scale. Because of such specific properties, this subject draws the attention of scientific disciplines such as physics, chemistry, and engineering.⁷ The one example of the application is molten metal filtration (see **Figure 1.10**). It is desirable that the ceramic foam used herein be resistant to both high temperatures, load of liquid flow and chemical corrosion.²⁰ In general, ceramics are hard and brittle materials with no electrical conductivity and low thermal conductivity.¹⁴ The thermal conductivity of ceramic foams is lower and mechanical properties are weaker than their dense state.⁴

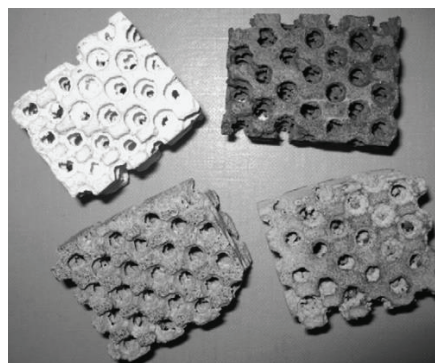


Figure 1.10. Produced ceramic foams for filtration of the molten metal (Source: Taslicukur, Z. et al., 2007).²¹

There are many publications about porous ceramic production methods in the literature. A recent review of the production methods of cellular ceramics (foams, honeycombs, fibers, hollows and rods) was published⁹ and a book on the production methods, properties and application areas of porous ceramics has been published.¹⁸ In addition, in the same years, an article is about the production methods of macroporous ceramics published.²⁰ The most primitive method of generating pores in ceramics is the sintering of coarse ceramic powders under favorable conditions.²² Monolithic porous structures are formed as a result of the contact surfaces of the particles are joined to prevent the neck region from annihilated by the gap between the powder particles.³ In addition to this method, there are three approaches that can provide more controlled and homogenous pore formation: replica technique, direct foaming and sacrificial templating.^{9, 20, 22} One of the most common ceramic foam production methods is the coating of the ceramic/liquid mixture into the strut of the open-cell polymer foam. This method was patented in 1963 by K. Schwartzwalder et al.²³ The process steps of open-cell ceramic foams with the replica method are as follows⁷:

- Preparation of slurry where ceramic powders are homogeneously distributed
- Impregnation of slurry with polymer foam
- Extraction of excess slurry
- Drying and/or Curing
- Removal of additives and polymer foam by heat treatment

After these processes, ceramic foam with positive replication of the open-cell polymer foam is obtained, so this method is called the replica method. In the replica method, it is very important to uniformly coating the struts of the foam. Since uncoated points or zones will remain empty after heat treatment, they affect the mechanical behavior of the foam in particular. One of the important points is the homogenous coating of the corner points of the polymer foam. Homogeneous uncoated corners will have a high-stress concentration during heat treatment.⁷ Increasing the stress concentration can lead to crack formation and subsequent breakage of the foam. Another point to note is that the temperature at which the polymeric foam decomposes during the heat treatment (sintering or pyrolysis) must be exceeded more slowly. This is because the gases resulting from the combustion of the polymeric foam cause the formation of stress when passing through the ceramic powder coating.⁹

The second ceramic production process is direct foaming. In the direct foaming process, gas bubbles are formed by mechanical, thermal or chemical ways in liquid (suspensions) containing the ceramic powders or preceramic precursors.⁷ After the gas bubbles formed the suspension or precursor must remain stable until the heat treatment (e.g. sintering). In the direct foaming method, there are three mechanisms that control the successful achievement of the ceramic foam.⁹ These mechanisms are drainage (drawing the liquid mixture or precursor towards the cell edges during solidification), coarsening²⁴ (gas bubbles joining to form larger bubbles and consequently larger bubbles grow, small bubbles disappear), the ceramic coating rupture (disruption of cell structure as a result of drainage and coarsening mechanisms). In order to prevent the formation of these mechanisms, gelation or crosslink formation is provided by using various additives.⁷ Coarsening with gelling or cross-linking is minimized.⁹ As an example of direct foaming method, foam concrete (gas concrete) can be given. After the addition of a foaming agent (aluminum powder, hydrogen peroxide, etc.) into the cement mixture, the foam structure is obtained by mixing. The aluminum powder used as the foaming agent reacts with water. As a result of this reaction, hydrogen gas is released. As the amount of hydrogen gas increases, the volume of foam concrete increases. Finally, curing under high pressure in the range of 170-200 °C is performed.²⁵⁻²⁶ As the final product, gas concrete with approximately a density of 0.4-0.8 g/cm³ is produced.²⁷ Unlike the replica technique, direct foaming method enables both open and closed pore production. In general, the pore size can be produced on a larger scale, but the strength of the foam decreases as the cell size increases. Therefore, stabilization of the bubbles is an important parameter. By changing the pore size, the total amount of porosity can be adjustable. In addition to this, because mostly interconnected pores are formed, foams with different permeability can be formed. Since the prepared suspension or precursor can be filled into any container, it is possible to produce foam in many different ways. It is difficult to control the production of cells in a single dimension or in graded dimensions, in homogenous form and open/closed pore.⁹

The third production method is sacrificial templating, in the sacrificial templating method, solid particles (synthetic organics, natural organics, salts, etc.) or liquid phases (water, oils, etc.) must be removed from the monolith structure. The particle in the structure leaves its own volume as a negative replica. In general, poregens are removed

from the body by using thermal and chemical methods. In both methods, regardless of the pore formers (salts, ceramics, metals, etc.), the matrix should have enough strength in the extraction step to prevent the collapse of the structure. When matrix is a suspension, the matrix strength must be ensured before setting up the pores by using setting agents. One of the differences between sacrificial templating and other porous ceramic production methods is that pore sizes, distribution and pore morphology can be created by selecting the desired poregen.²⁰ There is a wide range of literature on each of the aforementioned porous ceramic production methods. Furthermore, there are studies that produced ceramic foams by using different methods from the same material. For instance, a study shows that silicon oxycarbide ceramic foams can be obtained from preceramic using the direct foaming, the replica technique and the sacrificial templating.

In the following articles mechanical, electrical and thermal shock behavior of SiOC foam was investigated. In the first study, Si-O-C ceramic foam was obtained from polymeric foam system with the preceramic polymer. It has been shown that the mechanical strength of Si-O-C foams varies depending on the pyrolysis conditions (such as temperature and atmospheric conditions).²⁸ Results of the second article showed that the electrical properties of the porous ceramic are affected by the materials that make up the structure (such as SiC and C) as well as the additive materials (Cu).²⁹ In the third article, SiOC foams produced with traditional replica method have been shown to have lower thermal shock resistance than foams produced with direct foaming (polysiloxane/polyurethane solution). Results showed that thermal shock resistance depends on the strut structure of the foam, and as the density of the strut structure of the foam increases, the thermal shock resistance is increased.¹⁵ In the fourth study, SiOC foam, polymethyl methacrylate (PMMA) microbeads were used in silicon resin and produced by the sacrificial templating method. Results showed that mechanical strength depends on the cell size of the foam. As the cell size increases, the crack length required for fracture increases. Mechanical strength also increases.³⁰ The production of foams of the same compound by different methods helps to understand the effect of the production method on the properties of the foam. Based on the application area, there are also publications in which the requirements of ceramic foam are explained and examined. For example, the issues that should be considered in applications where ceramic foams were used as catalysts were investigated.³¹

1.2.1. Slip Casting

The suspension or precursor used in both direct foaming and sacrificial templating methods takes the form of the container. In other words, a forming method should be used to form the final product. Slip casting is a forming method which consists of a liquid phase, a solid phase, and additives. Slip casting is the shaping method in which advanced ceramics can be produced in complex shapes, fast and low cost. Due to the fact that the molds can be designed in desired shapes, it is possible to produce complex shapes easily. Gypsum (Plaster of Paris, $2\text{CaOSO}_4 \cdot \text{H}_2\text{O}$), which is used as a mold material, can be applied in the industry due to the low cost and reusability.³²⁻³³ In the slip casting method, the solid powder particles are distributed homogeneously in the appropriate liquid using various additives (binders, dispersants, etc.), this mixture is called slurry. The slurry is then poured into the gypsum mold, due to the capillary suction pressure (~ 0.15 MPa) of the pores in the gypsum mold, the liquid in the slurry is drawn into the mold. Meanwhile, the particles in the slurry also accumulate in the layer starting from the mold surface, this is called the cake formation (see **Figure 1.11.a**). After a while, the cake separates from the mold because of its own weight and it is called green body. Then, drying, binder burn out and firing processes are applied respectively and the final product is obtained.³³⁻³⁵

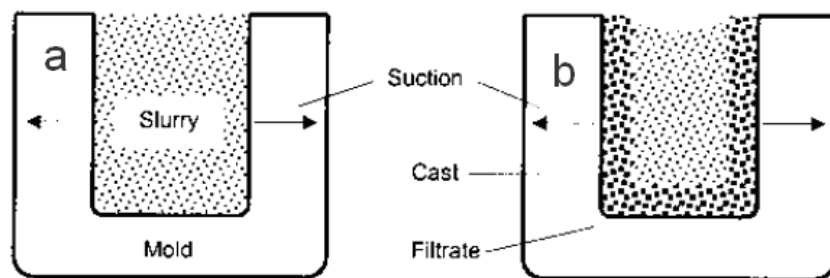


Figure 1.11. Schematic representation of the ceramic powder particles deposited on the mold surface during the absorption of the liquid in the slurry (Source: Rahaman, M. N., 2003).³⁴

The liquid in the slurry loses its speed both through the accumulated powder particles and through the mold. As a result of this, as the thickness of the parts increases,

it takes more time for the entire liquid to be absorbed by the mold.³⁴ Too much void is formed as the solid particles will randomly settle on the first accumulated surface between the mold and the piece. As the liquid in the middle of the casting is absorbed more slowly, the powder particles can be settled better. Therefore, the void ratio in the center of the part becomes less, the more homogenous structure is obtained (see **Figure 1.11.b**).³² The parameters such as the size, distribution, homogeneousness and the rate of compression of the powder particles in the slurry affect characteristics (density, mechanical properties, microstructure, etc.) of the green body and the final product after sintering. For instance, there may be voids in the product due to the non-homogeneous distribution of the lumps formed by small powder particles. Another example, solid particles with large and small sizes uses together because it is desirable to fill the voids between the large particles with small particles in the same slurry.³⁴ During the drying, shrinkage occurs due to the removal of the liquid. The cracks that may occur due to shrinkage. Several binders have been developed to prevent this situation.³⁶

The successful production of ceramic by the slip casting method is controlled by the properties of slurry, mold and ceramic powder particles. The main factors affecting the properties of the slurry are listed below³⁴:

- Solvents
- Dispersants
- Binders
- Plasticizers

Water is the most common solvent used in slip casting. However, there are also organic solvents used in the suspension. The advantages of the use of organic solvents are generally low surface energy, low vapor pressure, low boiling temperature, ability to dissolve organic additives. In solvent selection, the characteristic properties of the solvent, the relationship between powder and solvent, the relationship between additives and solvent, safety and cost are taken into consideration. The vaporization rate, which is one of the characteristic features of the solvent, is one of the important issues since it will change the solid/liquid ratio and rheology of the slurry during mixing and casting. Another condition is the soaking of the ceramic powders, the liquid wetting of the particle varies depending on the surface energies and the contact angle between the liquid phase and particle. If the solvent does not wet the ceramic powder particles,

undesirable conditions such as increased viscosity of the slurry may occur. Dispersants (i.e. deflocculants or dispersing agents) are basically described as additives which prevent the agglomeration of ceramic powders and thus ensure the uniformity of powder distribution throughout the slurry. The homogeneous distribution of ceramic powder particles is ensured by the regulation of van der Waals, electrostatic and steric forces. The balancing of the tensile and repulsive forces between the particles is controlled by dispersing agents.

The binders are polymeric materials which dissolve in the appropriate solvent and allow the particles within the slurry to attach together. In addition to binders such as poly (vinyl alcohol, PVA) which are soluble in water, there are also binders such as poly (vinyl butyral) which are soluble in organic solvents. The decomposition temperature of the binders is important due to mechanical strength decreases when the binder burnt out, the connections between the powder particles breaks off. Moreover, since the glass transition temperature of the binder is low, polymer chains generally have a less branched structure. Generally, the amount of binders is much more than other additive materials in slip casting. It is therefore desirable to use the appropriate amounts for not affecting the properties of the slurry. The polymerization rate of the binders must also be taken into account, the rapidly polymerizing binders can alter the rheology of the solvent and can cause the casting not to occur. Plasticizers are used to provide flexibility to the green body by changing the strength that the binders are provided to the green body.³⁴

As mentioned before, the flow rate of the liquid phase in the slurry influences all the properties of both the green body and the final product. The flow of the liquid in the slurry (J) depends on the capillary suction pressure generated by the mold, the permeability of the porous medium (K), the pressure gradient (dp/dx) formed in the liquid, and the viscosity (η_L) of the liquid. As shown in Darcy's law (Equation 1.4), the flow of liquid increases as the capillary suction pressure, porous medium permeability, and pressure gradient increase. As the viscosity of the liquid increases, the flow of the liquid decreases.³⁴

$$J = K \cdot \left(\frac{dp}{dx}\right) / \eta_L \quad (1.4)$$

1.3. Calcium Silicate Hydrates and Porous Calcium Silicates

In general, calcium silicate hydrates are known as the binder phase in the cement industry.³⁷ The purpose of the amorphous calcium silicate hydrate (CSH) phase in the hardened cement ensures the strength of the structure under ambient conditions.³⁸⁻³⁹ There are more than thirty CSH phases known in the literature.⁴⁰⁻⁴¹ The wide range of the Ca/Si ratio allows the production of various calcium silicate. Calcium silicates are not affected by only Ca/Si ratios, but also production conditions affect the calcium, silicon, hydrogen, and oxygen content of the final product.^{39, 41}

Xonotlite is a calcium silicate hydrate compound containing Ca and Si in a ratio of about 1:1.⁴²⁻⁴³ The chemical expression of the xonotlite is $\text{Ca}_6\text{Si}_6\text{O}_{17}(\text{OH})_2$ or $\text{C}_6\text{S}_6\text{H}$.⁴⁴ Xonotlite was discovered by K. F. A. Rammelsberg in 1866. "Xonotlite" is named after its discovery territory, Tetela de Xonotla, Mexico.⁴⁵ Xonotlite is used in many applications such as thermal insulation and fireproofing due to its stability up to medium temperatures (about 600 °C).⁴⁴ In the hydrothermal synthesis method, xonotlite is obtained by reacting the suspension of Ca source and Si source under certain temperature and pressure. The shape of the xonotlite formed as a result of the hydrothermal synthesis can be either needle-like (see **Figure 1.12**) or spherical.⁴³ The temperature required for the production of needle-like xonotlite with the hydrothermal synthesis method is generally above 200 °C.⁴³

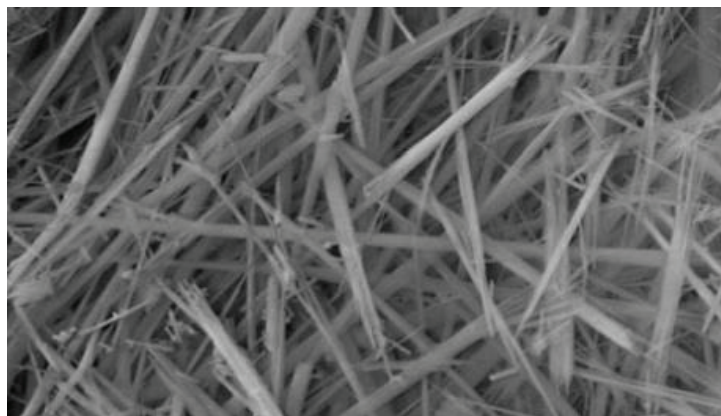


Figure 1.12. SEM image of the needle shape xonotlite (Source: Black, L. et al., 2009).⁴⁵

Although it seems like a simple procedure, production of the single-phase xonotlite with high purity is a complex process due to the metastable phases formed during the

production. For instance, in hydrothermal synthesis, xonotlite and tobermorite can be produced with Ca: Si ratio between 0.8 and 1. The temperature of the hydrothermal synthesis determines the compound to be formed. As shown in **Figure 1.13**, when the temperature of the hydrothermal synthesis is above 140 °C xonotlite may occur; on the other hand, below the 140 °C, tobermorite may occur.⁴¹

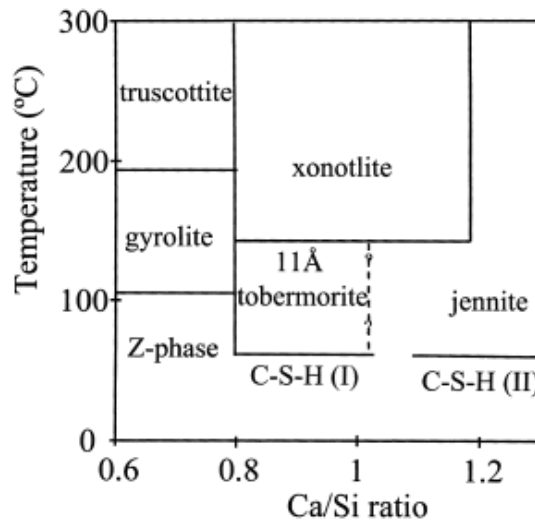


Figure 1.13. Schematic diagram of the CSH materials zone (Source: Shaw, S. et al., 2000).⁴¹

Wollastonite is a calcium silicate compound with chemical formula CaSiO_3 or $\text{CaO} \cdot \text{SiO}_2$ and theoretical density of 2.9 g/cm^3 . Its hardness is in the range of 4.5-5 Mohs hardness. Wollastonite is used in many applications such as traditional ceramic⁴⁶, biomaterial⁴⁷, high-frequency insulation⁴⁸ and polymer composite applications.⁴⁹⁻⁵⁰ The purpose of the use in traditional ceramics is to reduce shrinkage, it is used in biomaterial applications because of being biocompatible nature of the wollastonite, and the reason for its use in polymer composites is to the enhancement of the mechanical properties. The reason for selecting wollastonite for the development of mechanical properties is that medium Mohs hardness value and good filler behavior due to it is a needle-like shape with a high aspect ratio (average length-to-diameter ratio 15:1).⁵⁰ Wollastonite is usually obtained by heat treatment from a calcium silicate hydrate (such as xonotlite, tobermorite). During the heat treatment, the chemically bound water in the xonotlite structure is separated at 700-800 °C and the xonotlite becomes wollastonite.^{48, 51-52}

In the literature, the production of porous monolithic wollastonite has been studied rarely. In a study⁵³, xonotlite/zeolite porous monolith was produced. For the production of the porous monolithic xonotlite/zeolite, polymethylmethacrylate (PMMA) was used as porogen. During the heat treatment, the PMMA burned away (~400 °C), thus pores were formed in the structure. The thermal behavior of xonotlite in the structure was investigated and it was seen that physical water was separated at 200 °C. When the temperature reached 800 °C, all of the xonotlite transformed into wollastonite (see **Figure 1.14**). The difference between initial weight and final weight after heat treatment was below 10%. It is stated that the porous structures produced contain approximately 86% porosity.

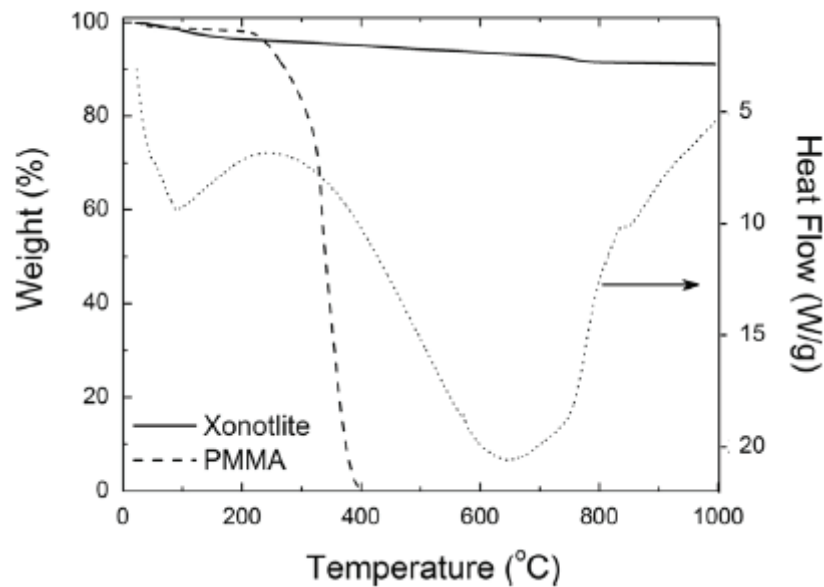


Figure 1.14. Illustration of the thermal gravimetric analysis of Xonotlite and PMMA (Source: Vakifahmetoglu, C., 2014).⁵³

Some researchers studied that the improvement of the strength of the porous wollastonite structure by adding Mg.⁵⁴ The porous Mg-wollastonite monoliths were produced as biomaterials in the substitution of the bone scaffold. Porous structures were manufactured by the 3D printing method. Mg-doped wollastonite suspension was used as ink. According to the Mg amounts (0-3.5 wt% wollastonite) of Mg-wollastonite structure, total porosity of the porous monoliths were 50-60%. Additionally, it was seen that the compressive strength of the porous monoliths was over 120 MPa. Another

example of porous monolithic wollastonite applications was carried out⁵⁵, polyethylene glycol was used as porogen to produce porous wollastonite parts. The effects of pore size and porosity on mechanical behavior were investigated using PEG in different sizes and quantities. It was seen that the porosity was ranged from 41.28% to 73.60%. Porous monoliths having a compressive strength of 4.92 MPa to 65.21 MPa were obtained depending on the porogen amount and size.

1.4. Aircraft Arresting Systems

Despite developments in aviation, accidents still occur and cause a loss of life. Technical or environmental factors may lead to accidents. In the case of aircraft that fail to stop along the runway distance during take-off or landing, such accidents are called overrun.⁵⁶ To reduce overrun damage, the Federal Aviation Administration (FAA) of United State of America (USA) has made it necessary to add a Runway Safety Area (RSA) of 305 m to both ends of the runways based on accident statistics.⁵⁶⁻⁶⁰ However, many airports cannot implement the Runway Safety Area (RSA) due to environmental factors (natural or man-made obstacles). Some suggestions have been put forward because of these obstacles.⁵⁸ One of the suggestions is Soft-Ground Arresting Systems (SGAS). In the case of overrun, when aircraft enters to SGAS, the drifting force occurs in the opposite direction to the aircraft's movement. The kinetic energy of the aircraft is transferred to such arresting material. Accordingly, the aircraft slows down and stops as a result of this situation. The arresting mechanism operates with the aircraft's weight without the need for any external energy source. Some advantages&disadvantages of common SGAS materials are given in **Table 1.1**.⁶¹ The Engineered Arresting System Corporation (ESCO) has conducted studies on the development of lightweight, frangible concrete with high-energy damping.⁶² Engineered Material Arresting System (EMAS), which consists of low density ($0.32-1.9 \text{ g/cm}^3$)⁶³ and high crushable concrete, was developed by the ESCO in the 1990s.

Due to structure and the formation of pores, the mechanical properties of the foamed concrete decrease.⁶⁴ The compressive strength of the foamed concrete should be lower than the stress caused by the aircraft's weight ($\sim 207 \text{ kPa}$)⁶⁵. On the other hand, the compressive strength of the foamed concrete should be able to carry emergency vehicles and survivors after the overrun accident.⁶⁶ Because of these special

requirements, the compressive strength of the foamed concrete must be considered. Therefore, the compressive strength of the foamed concrete depends on the amount of pore in the concrete and thus density.⁶⁷⁻⁶⁸

Table 1.1. Advantages and disadvantages of Soft-Ground Arresting Systems ⁶¹

Passive Arresting Material	Advantages	Disadvantages
Gravel	Economical and easy to supply	Suitable for use only in good weather conditions and the ricochet off the material can damage the aircraft.
Soft soil, sand, and clay	Economical and easy to supply	Difficult to control physical properties in various weather conditions
Water pool system	A system that can be used continuously without the need for additional expenditure	Can only be used in good weather and difficult to prepare
Phenolic Foam	Easy to set up, stable physical properties, and good fracture behavior	A system to be repaired after each use
Foam concrete	Easy to set up	Abrasive properties can damage the aircraft

The load formed by the weight of the aircraft breaks and compresses the foamed concrete when the aircraft enters EMAS (see **Figure 1.15**). The drag force takes place between the compressed concrete and the aircraft wheels.

The aircraft stopping distance is inversely proportional to the amount of energy absorbed by the foamed concrete. As the amount of energy which will be absorbed during the foamed concrete breaking increases, the stopping distance of the aircraft reduces.^{56, 69} The area under the stress-strain curve (see **Figure 1.16**) shows the amount of total energy absorbed.

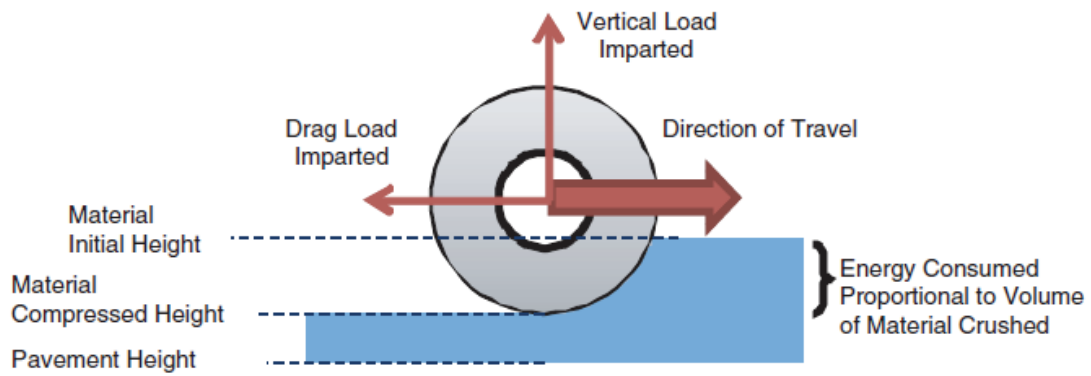


Figure 1.15. Schematic illustration of the aircraft wheel and forces formed into the EMAS (Source: Heymsfield, E. et al., 2007).⁷⁰

In addition to the benefits of foamed concrete used as EMAS, there are disadvantages. These disadvantages are setup cost⁶², the high maintenance cost⁶², the time to repair is 45 days after the overrun⁶⁵, the difference between the length of the RSA field applied to one end of the runway (305 m) and the total length of EMAS (289.6 m).

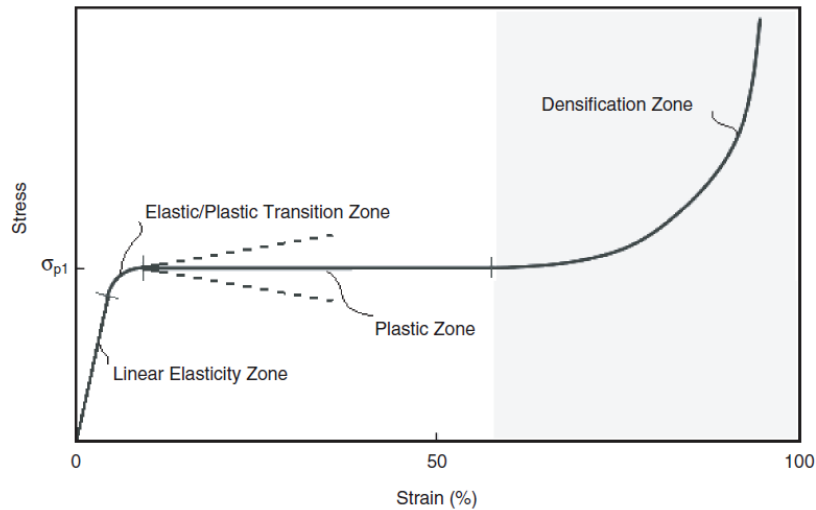


Figure 1.16. The stress-strain diagram of the foamed concrete (Source: Santagata, E. et al., 2010).⁷¹

There are many studies in the literature related to EMAS. These studies are included documents such as articles, book chapters⁶⁸, and reports^{61, 70, 72}. In addition to the research and development of EMAS materials, computer programs have been

developed and simulations of EMAS applications that can be used in overrun accidents have been studied. Simulations also confirmed the studies and showed that the density of foamed concrete is the main factor affecting the stopping distance.^{65-66, 69} In general, most studies are intended to modify the composition of EMAS or to change the design of EMAS to reduce RSA.^{66, 73-74} In addition to all these foamed concrete-oriented studies, there were also studies for producing porous parts with the necessary properties for EMAS using different materials. In one of these studies⁷⁵, kaolin, talc powder and alumina are the main materials. Animal protein was used as the pore-forming agent in the production of monolithic porous materials. The results showed that porous monoliths which have different pore size and porosity had that a compressive strength in the range of 0.19 to 4.89 MPa. These compressive strength values were ideal for use as EMAS material.

The results show that it was possible to produce aircraft arresting materials using materials other than foamed concrete. In the present study, monolithic porous materials will be produced using xonotlite powder. The suitability of these porous monoliths as an EMAS will be investigated. In particular, the compressive strength behavior and the measured porosity will be investigated in depth.

CHAPTER 2

EXPERIMENTAL PROCEDURE

2.1. Used Raw Materials

In present studies, porous calcium silicate monoliths (wollastonite, CaSiO_3) were produced from commercial calcium silicate hydrate powder (xonotlite, $\text{Ca}_6\text{Si}_6\text{O}_{17}(\text{OH})_2$, 49.1 % SiO_2 , 42.2 % CaO , Promaxon D, Promat International NV, Tisselt, Belgium) and some additives were used such as Dolapix CE 64 (Zschimmer & Schwarz GmbH & Co., as a dispersing agent), poly-vinyl alcohol solution (PVA, Sigma-Aldrich, M_w 31000, as a binder), Polymethylmethacrylate microbeads (PMMA, as a sacrificial pore former). As a slip casting mold material, gypsum (Plaster of Paris, $2\text{CaOSO}_4 \cdot \text{H}_2\text{O}$) was used.

2.2. Production of Gypsum Mold

First of all, in borosilicate glass beaker, 700 ml distilled water (DI water), 1 kg gypsum was added slowly and it was mixed by hand for homogeneous mixing the powders without agglomeration. After all the gypsum was added in to the blend, it was mixed for (5 min). Second, for casting the model was fixed in a container where the casting would take place. Soap coating was applied to walls of the container to be cast and the surfaces of the model to prevent from sticking after the casting. Then, the gypsum slurry was poured into the prepared negative mold. During the casting, the container was shaken for a while to remove the entrapped gas in the gypsum slurry and was left for 24 h at RT and then removed from the negative mold. At the same time, the model was taken out of the casting mold. Prior to use to formed mold, it was dried for 14 days at RT. The dimensions of the gypsum mold cavity (see **Figure 2.1**) was measured as 105 mm x 65 mm x 17 mm.

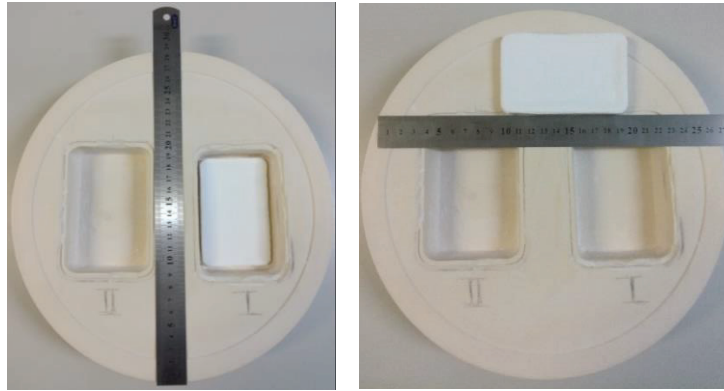


Figure 2.1. Photographs of gypsum mold and green body of calcium silicate hydrate sample.

There are some significant points in the production of gypsum mold for the slip casting technique. For instance, it should be ensured that all surfaces of the model should completely be coated with soap. Because gypsum sticks to unsaponified surfaces and it may cause surface defects. The slurry should be mixed well after adding all the gypsum powder into the water. If agglomerates stay in the slurry, after casting, it may generate stress in the cake and lead to crack formation. As the amount of water used in gypsum slurry increases, the amount of porosity in the walls of the mold increases. This leads to an increase in the capillary suction of the mold. It should be noted, however, that it causes non-homogeneous particle accumulation when water is quickly removed from the body. As a consequence, tensile stress and cracks may form in the body.

Besides the influences of the mold characteristics, the size of the gypsum mold and the amount of slurry are important due to the body should have sufficient strength to bear its weight. If the body's thickness is not sufficient to provide this strength, it usually breaks while removing the body from the mold. The required thickness of the green body varies depending on the part's width and length. The water inside the slurry will begin to be absorbed during the slip casting from the first point it contacts the surface of the mold. This means that if the all slurry is poured to the same point of the mold, a very non-homogenous and layered structure occurs to owe to inadequate mold surface absorption. Also, sudden slipping of the whole slurry into the mold may create problems such as splashes and non-homogeneous particle distribution.

2.3. Production of Porous Calcium Silicates

Preliminary experimental studies were performed to determine the optimum amounts of Xonotlite and PVA solution. The total volume of the suspension prepared for slip casting was 100 ml and the amount used of chemicals in the preliminary experimental design are shown in **Table 2.1**. Before the suspension preparation, PVA solution was prepared as followed steps: (i) PVA added in the water, (ii) the mixture was mixed by magnetic stirrer for 10 min at 150 rpm and at 85 °C, (iii) after PVA totally dissolved in water, suspension cooled to RT, (iv) for preventing the change of percentage of PVA solution, the amount of water evaporated during mixing was added to the solution.

For the preparation of preliminary experimental suspension, firstly the specified amount of distilled water was poured into the glass beaker, then Dolapix CE 64 was added and the mixture was stirred for 5 min at a stirring speed of 100 rpm. Dolapix CE64 was added in the suspension according to the xonotlite 1.5% by weight. After the mixture was homogenized, PVA solution was added to the mixture. The PVA solution was selected as the binder. The mixing speed was then elevated from 100 rpm to 750 rpm for a smooth dispersion and for no agglomeration, then xonotlite was slowly added to the mixture.

After all chemicals were added, the beaker was sealed (to prevent water loss) and stirred at a stirrer speed of 750 rpm for 3 h by a magnetic stirrer (Weightlab Instruments, WN-H550 magnetic stirrer). When ball milling was applied instead of a magnetic stirrer, a very dense mixture (creamy suspension) was obtained which was not suitable for casting. After 3 h mixing, the suspension was poured into the gypsum mold and allowed to dry at RT for 24 h. After 24 h of monolithic samples removed from the gypsum mold and were allowed to dry at RT for 72 h. Unfortunately, large cracks occurred on the surfaces of the first samples which contained 4% and 6% (by volume) (see **Figure 2.2**) shown in **Table 2.1** after casting processes.

In order to avoid these crack initiators, the amount of the xonotlite was increased in the next sets to 8, 9, and 10% (by volume) xonotlite were obtained. These samples made from 8, 9, and 10% xonotlite (by volume) were selected for further experiments. Since they did not crack, in addition to optimiza the amount of xonotlite, experiments were

also carried out to increasing the percentage of PVA solution. It was seen that when the amount of PVA was less than 5% by weight of the xonotlite, cracks were formed in the samples. Therefore, it was decided to use a 5% wt PVA solution in next experiments. All investigated samples are tabulated in **Table 2.1**.

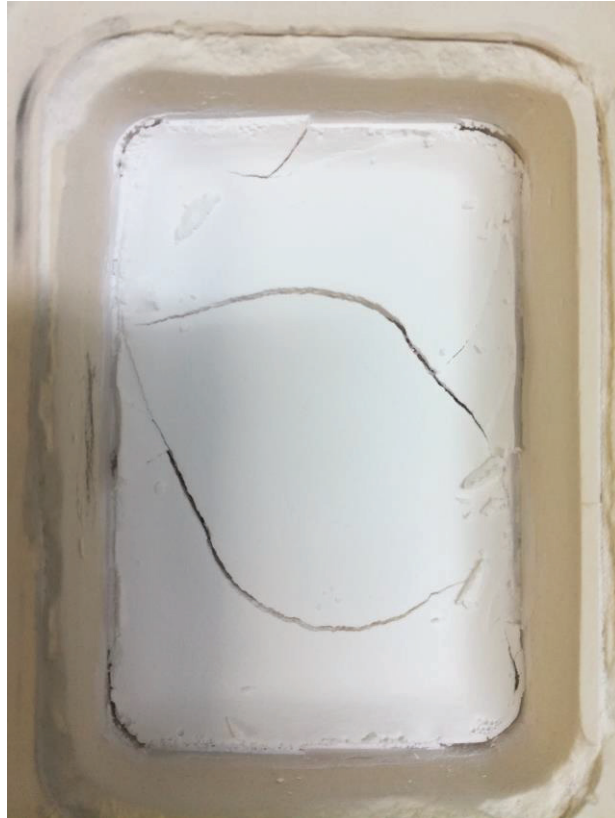


Figure 2.2. Photograph of the sample which has large cracks.

Sets containing 8, 9, and 10 vol% xonotlite (by volume) were selected to form porous monolithic samples. Polymethylmethacrylate microbeads were used as the porogen. PMMA was added into suspension after xonotlite. In the experimental design, the amount of PMMA was determined as xonotlite to PMMA ratio by volume being no PMMA, 1, 0.82, 0.54, and 0.33. Experiments with a ratio of xonotlite: PMMA 0.18 could not be carried out except the suspension containing 8% xonotlite, because adding PMMA increased the density of the mixture and prevented the suspension to mixed well.

Table 2.1. Chemicals used for casting suspension in preliminary experiments.

Sample Code	Xonotlite (ml)	PVA (g)	Dolapix CE 64 (g)	Distiled water (ml)
SC 1	4	0.52	0.156	95.40
SC 2	4	0.208	0.156	95.68
SC 3	4	-	0.156	95.87
SC 4	6	0.78	0.234	93.15
SC 5	6	0.312	0.234	93.52
SC 6	6	-	0.234	93.81
SC 7	8	1.04	0.312	90.80
SC 8	8	0.416	0.312	91.37
SC 9	8	-	0.312	91.74
SC 10	9	1.17	0.351	89.65
SC 11	9	0.468	0.351	90.28
SC 12	9	-	0.351	90.71
SC 13	10	1.3	0.390	88.50
SC 14	10	0.52	0.390	89.21
SC 15	10	-	0.390	89.68
SC 16	11	1.43	0.429	87.36
SC 17	11	0.572	0.429	88.13
SC 18	11	-	0.429	88.64

The experimental matrix and component amounts of the PMMA-used sets are shown in **Table 2.2**. Suspensions containing 11% xonotlite in volume were tested with PMMA, but due to the increased amount of PMMA, the viscosity of the suspensions was increased. Therefore casting of the suspension could not be conducted. Samples were separated from the gypsum mold after 24 followed casting. Then the samples were left at RT for 72 h to dry completely. After the samples were completely dried, heat treatment was applied to remove the PMMA. The schematic view of the production procedure of porous monoliths gave in **Figure 2.3**.

Table 2.2. Raw materials used in porous monolithic sample production.

Sample Code	Xonotlite (ml/g)	PMMA (ml/g)	PV A (g)	Dolapix CE 64 (g)	Distiled water (ml)	Vol.% of xonotlite/PMMA
A1	8/20.8	-	1.04	0.312	90.80	-
A2	8/20.8	8/9.44	1.04	0.312	90.80	1
A3	8/20.8	9.78/11.54	1.04	0.312	90.80	0.82
A4	8/20.8	14.86/17.53	1.04	0.312	90.80	0.54
A5	8/20.8	24/28.32	1.04	0.312	90.80	0.33
B1	9/23.4	-	1.17	0.351	89.65	-
B2	9/23.4	9/10.62	1.17	0.351	89.65	1
B3	9/23.4	10.98/12.96	1.17	0.351	89.65	0.82
B4	9/23.4	16.71/19.72	1.17	0.351	89.65	0.54
C1	10/26	-	0.52	0.390	89.21	-
C2	10/26	10/11.8	0.52	0.390	89.21	1
C3	10/26	12.22/14.42	0.52	0.390	89.21	0.82
C4	10/26	18.57/21.91	0.52	0.390	89.21	0.54

During the heat treatment (see **Figure 2.4**), the furnace (Protherm PEF series PC442 electric furnace) was heated from RT to 400 °C with 2 °C/min and 1 h dwelling time.

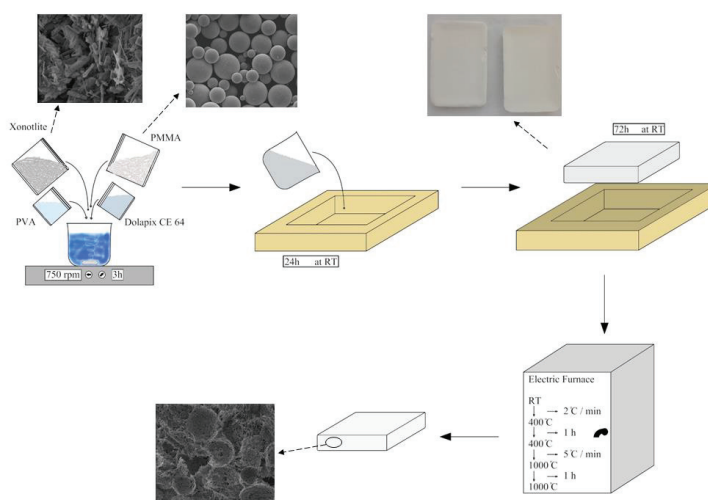


Figure 2.3. The schematic diagram of the production procedure.

At this step, the PMMA and additives burned away from the monolithic structure.⁷⁶⁻⁷⁷ Then the furnace was heated from 400 °C to 1000 °C with the heating rate (5 °C/min). Finally, porous monolithic samples were kept at 1000 °C for one hour and then were cooled in the furnace.

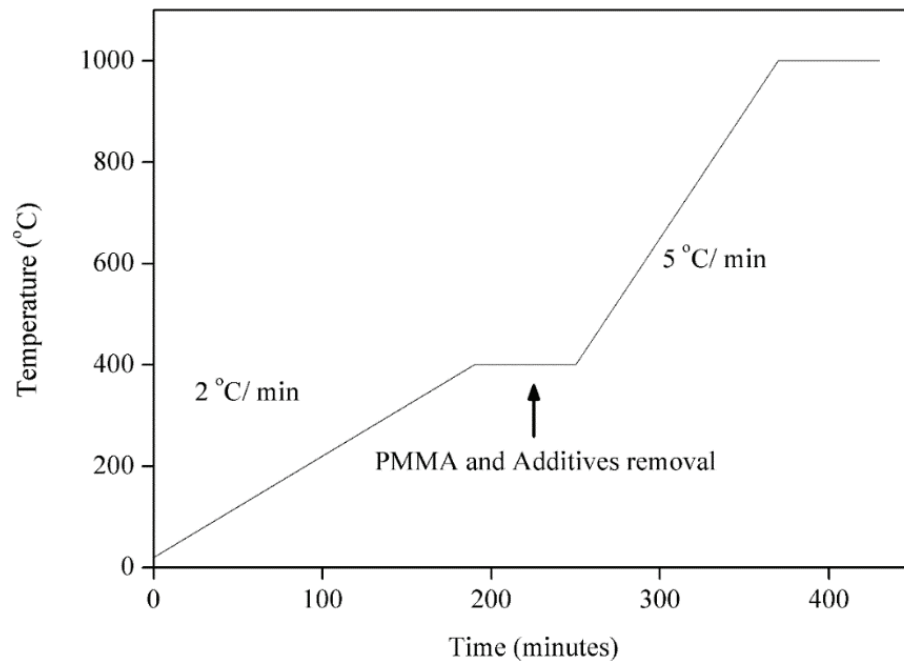


Figure 2.4. Diagram showing heat treatment in terms of temperature and time.

2.4. Characterization

The characterization analysis (microstructural, structural and mechanical) of the porous monoliths were conducted.

2.4.1. Microstructural Characterization

The microstructural analysis was performed to investigate the shape and size of the pores in porous monoliths. **Equation 2.1**⁷⁸ was used to calculate the diameters of three-dimensional pores from two-dimensional images taken from SEM. The other objectives of the microstructure analysis are the distribution behavior of PMMA microbeads and xonotlite particles in porous parts. Philips XL 30S FEG Scanning Electron Microscope (SEM)- Secondary electron detector was used for the microstructural analyses. Before

microstructural analyses, broken surfaces of all porous monoliths were coated by an Au layer.

$$d_{sphere} = \frac{d_{circle}}{0.785} \quad (2.1)$$

2.4.2. X-Ray Diffraction Characterization

X-ray analyses were used to investigate the phases of the ceramic powder in the structure of the starting materials and the samples before and after heat treatment. All phase analyzes of the powder samples were performed on the Philips X'Pert Pro instrument. In X-Ray diffraction analysis, the range of angle 2θ was applied from 10° to 90° and the scan step was $0.005^\circ/\text{second}$.

2.4.3. Mechanical Characterization

The purpose of the mechanical analysis of porous monolith parts is to investigate the convenience of porous parts as aircraft arresting material. Cold Crushing Strength (CCS) of the monolith samples was determined by test procedure which specified in ASTM Standard C773-88.⁷⁹ The cold crushing strength test specimens used in AG-I 250 kN Shimadzu mechanical test machine were cubes which have edge dimensions of 10 mm x 10 mm x 10 mm. In the application of the cold crushing test, the samples placed between two platens parallel to each other were compressed along the loading axis. The crosshead speed was set up as 1 mm/min. The test set up is shown in **Figure 2.5**.

$$CCS = \frac{P}{A_0} \quad (2.2)$$

The compressive strength values of the porous samples were obtained using **Equation 2.2**.

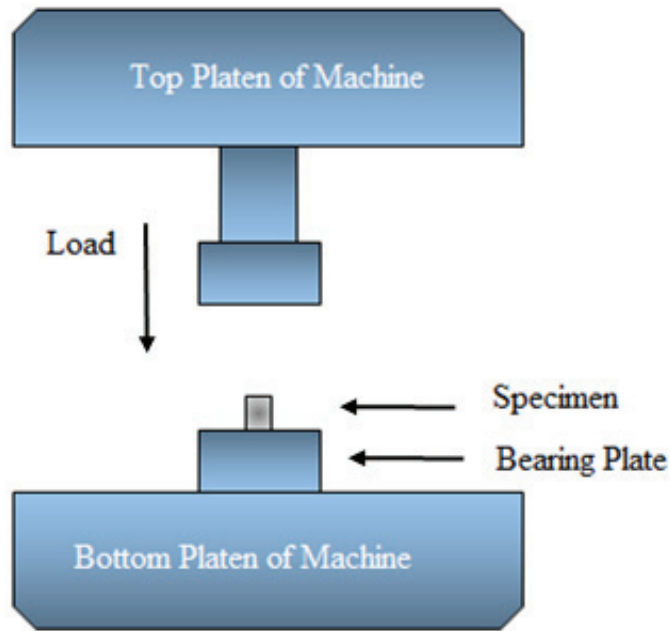


Figure 2.5. Illustration of the Cold Crushing Strength test set up.

2.4.4. Thermogravimetric Characterization

Decomposition of the PMMA or phase transition temperature of the xonotlite is analyzed by thermogravimetric analysis (TGA, Shimadzu TGA-51). The TGA samples were heated from RT to 1000 °C with a 5 °C/min heating rate in air. The TGA was conducted to determine both the temperature of the physically and chemically bound water removed in the xonotlite structure and the temperature of PMMA decomposition which used as the former sacrificial pore.^{44, 53} Identifying these temperatures is important to determine the temperatures of the heat treatment process.

CHAPTER 3

EXPERIMENTAL RESULTS & DISCUSSION

3.1. Raw Materials

The microstructural analysis was conducted by using SEM. **Figure 3.1.a** shows that the shape of the xonotlite particles which is needle-like with particle length below 4 μm and width below 1 μm . **Figure 3.1.b** indicates that the shape of the PMMA particles was spherical.

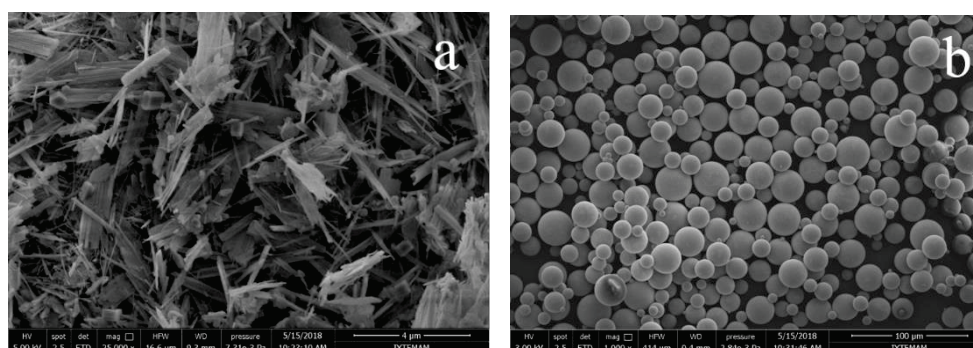


Figure 3.1. SEM images of the xonotlite (a) and the PMMA (b) particles.

The average diameter of the spherical PMMA particles obtained from SEM images as $17.78 \pm 0.56 \mu\text{m}$ by using computer software (Image J). **Equation 2.1** was used to convert the diameters taken from two-dimensional SEM images to three-dimensional. The calculated three-dimensional average diameter of the spherical PMMA particles was $22.65 \pm 0.71 \mu\text{m}$. Also, the Malvern Mastersizer 2000 was used to investigate the distribution of particle size PMMA. It can be seen that from **Figure 3.2**, the average diameter of the PMMA particles is between $19.95 \mu\text{m}$ and $26.30 \mu\text{m}$.

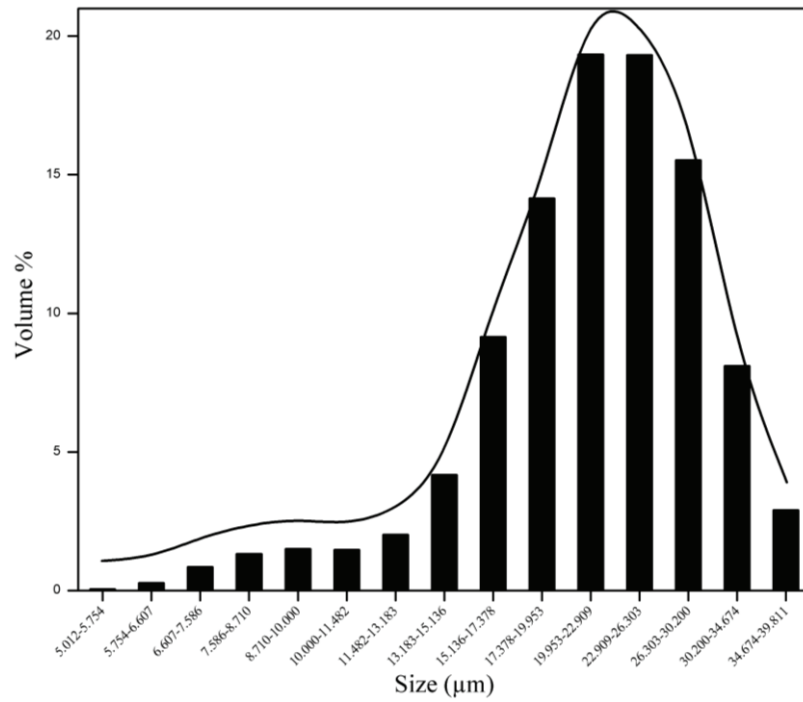


Figure 3.2. The particle size distribution of the PMMA particles.

The XRD pattern of the xonotlite before heat treatment, was shown in **Figure 3.3**. The 2θ values of characteristic xonotlite phase peaks were observed at 20.93° , 24.50° , 27.50° , 28.96° , 31.68° , 33.11° , 35.78° , 38.52° , 40.05° , 44.48° , 46.56° , 49.54° , and 53.41° , seen in **Figure 3.3** (ICDD No 23-0125). When the temperature of the system reaches to approximately 700°C , these characteristic peak disappears due to phase transformation xonotlite to wollastonite.⁵³

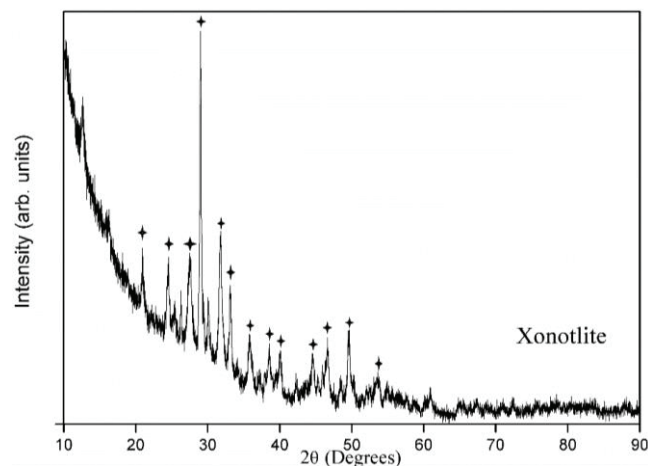


Figure 3.3. The X-Ray Diffraction pattern of the pure xonotlite powder.

Finally, Thermogravimetric analysis results of the raw materials were presented in **Figure 3.4**. According to **Figure 3.4**, from 50 °C to 200 °C, the xonotlite mass reduction were only 4 %, this mass reduction associated with the loss of water that was physically bonded.⁴⁴ In addition, there was a mass reduction of about 3 % between 600 °C and 700 °C, due to the loss of chemically bonded water in the xonotlite structure. Over 700 °C xonotlite calcination occurred and the xonotlite phase transformed into the wollastonite phase. Through the high thermal stability of the wollastonite between 700-1000 °C, mass reduction was lower than 1%. On the other side, as a sacrificial pore former, the PMMA decomposed almost entirely between 300 °C and 400 °C.

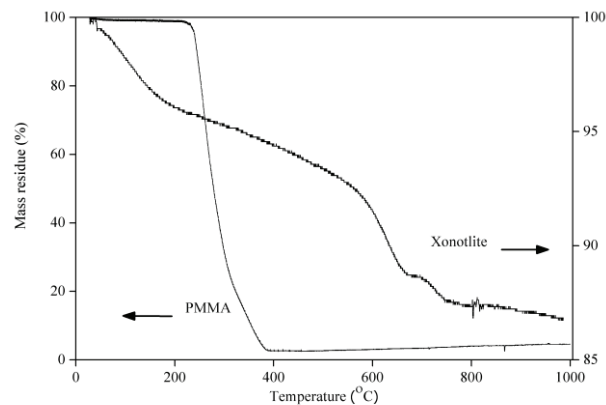


Figure 3.4. Illustration of the TGA of the xonotlite and PMMA.

3.2 . Porous Monoliths

The characterization results of the porous monoliths was presented in this chapter.

3.2.1. Microstructural Analysis

As stated in **Chapter 2.2** and **Table 2.2**, there was no PMMA in the first set (i.e. A1, B1, and C1). The SEM images of fractured surfaces of monolith which contained 8 vol% xonotlite (by volume) and no-PMMA are shown in **Figures 3.5.a and b**. As seen

in **Figure 3.5.a**, during heat treatment process wollastonite particles fused with each other and formed around 40 μm diameter structures.

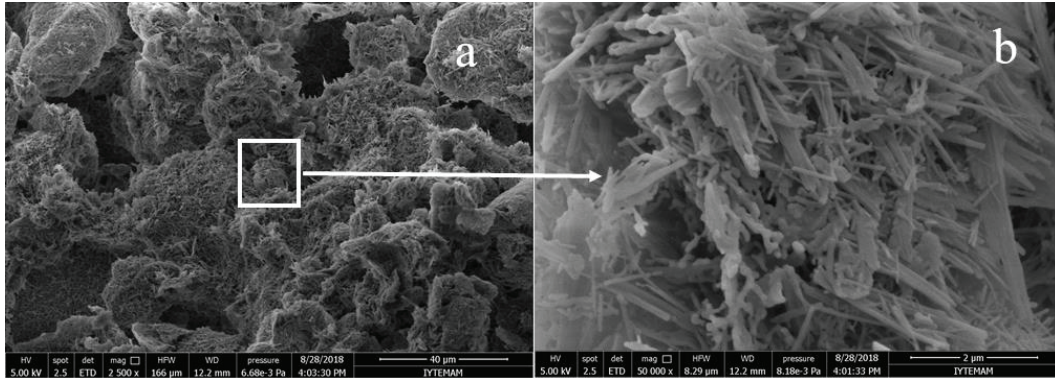


Figure 3.5. The SEM images of the monolith part with no-PMMA.

Beside that interparticle porosity, there were voids in between needle-like wollastonite particles on the agglomerates (see **Figure 3.5.b**). Also, it can be seen that from **Figure 3.5.b**, there needle-like xonotlites kept their shape while transforming to wollastonite.

Figures 3.6.a-d and insets show the SEM images of A2, A3, A4, and A5 which were comprising PMMA (with 1, 0.82, 0.54, and 0.33 xonotlite to PMMA ratios, respectively). The SEM images of the porous microstructure revealed that there were two types of macroporosity. The first one was formed between by the decomposition of the spherical PMMA particles having average cell size of 20 μm . The second one was created needle-like wollastonite particles. Increasing the PMMA content, which means reducing the volumetric xonotlite to PMMA ratio from 1 to 0.82, 0.54 and 0.33, led in much-improved interconnectivity between the cells owing to the enhanced amount of contact points between the PMMA particles after slip casting. However, this has also led to thinner struts and the presence of flaws as well. **Figures 3.7.a-c** demonstrates SEM pictures of fractured surfaces of A4, B4, and C4 that was consisting of 8, 9, and 10 vol% xonotlite, respectively. The xonotlite to PMMA ratio in these sets remained constant as 0.54. The SEM images with low magnification were taken for general information about the pore distribution and insets were taken for interpreting to distribution of the wollastonite particles between PMMA beads.

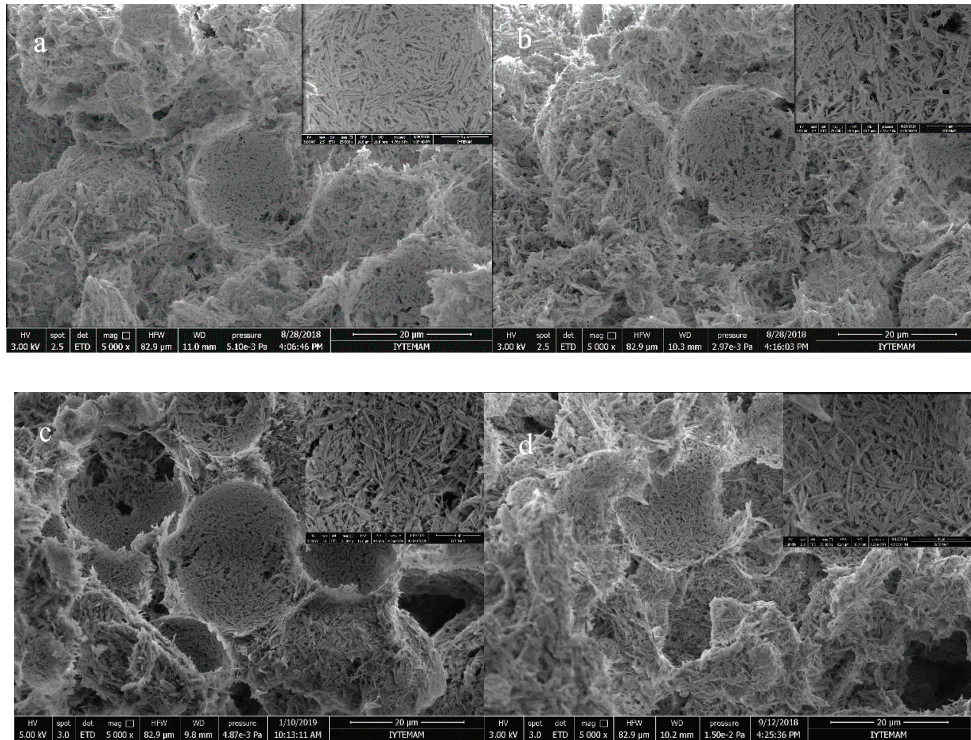


Figure 3.6. The SEM images of porous monoliths with decreasing xonotlite to PMMA ratio by 1, 0.82, 0.54 and 0.33, respectively.

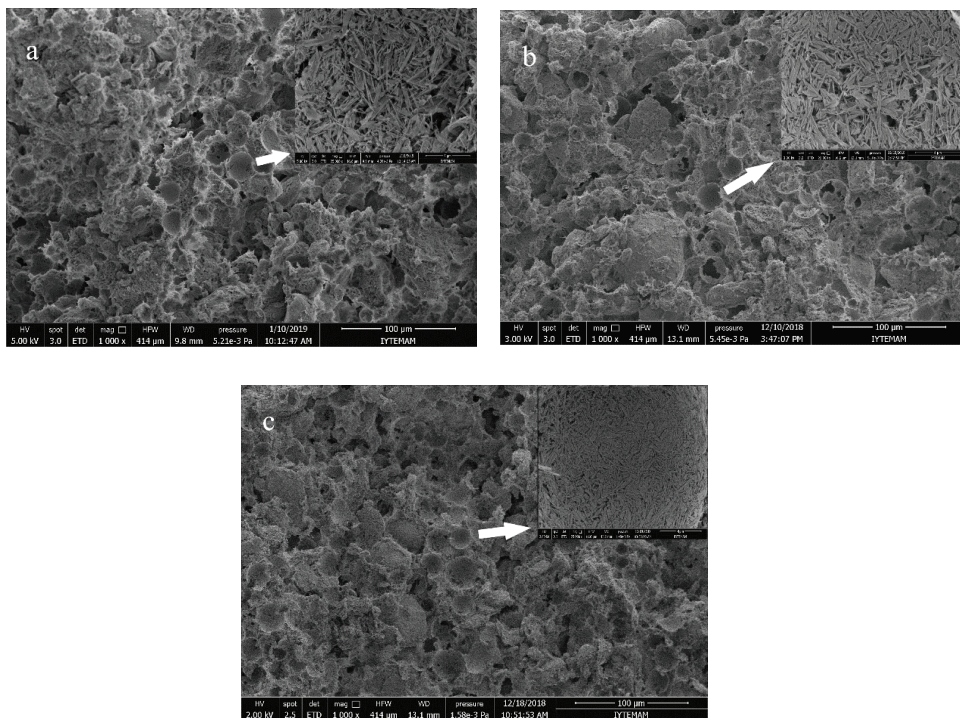


Figure 3.7. The SEM images of porous monoliths (A4, B4, and C4) with constant xonotlite to PMMA ratio (0.54) and increasing xonotlite content.

When the xonotlite volumetric content increased from 8 to 9 then 10, change in the pore distribution was not clearly observed. Beside that SEM images of inset indicated that particle packaging and distribution improved with increasing content of xonotlite. Due to the improvement of the packaging, it can be seen that voids between wollastonite particles was decreased.

3.2.2 . Structural Analysis

The X-Ray Diffraction analysis was carried out on the wollastonite powders, that were obtained from porous monolith parts after heat treatment at 1000 °C, for the demonstration of the phase transition between the xonotlite and the wollastonite. **Figure 3.8** shows the X-Ray Diffraction patterns of A, B and C series. **Figure 3.8** shows that the phase transition between the xonotlite and the wollastonite (ICDD No 43-1460) occurred after applying heat treatment to all specimens.

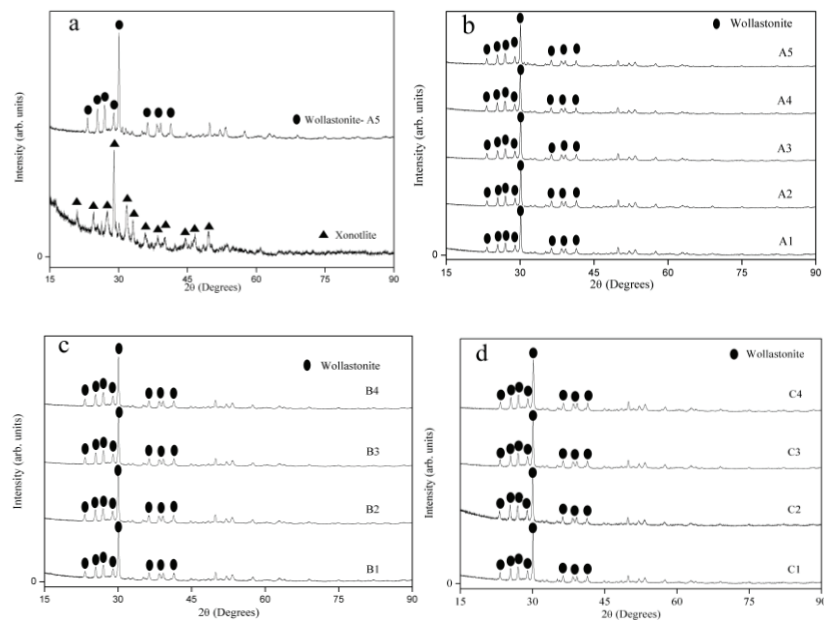


Figure 3.8. The XRD patterns of xonotlite and A5 samples (a) and A (b), B (c) and C (d) series after thermal treatment.

If **Figure 3.3.a** is examined, it can be seen that xonotlite-related peaks disappeared and wollastonite-related peaks showed up after heat treatment.^{48, 53} This characteristic peaks were identified as 23.14°, 25.28°, 26.84°, 28.86°, 29.98°, 36.17°, 38.20° and 39.02° from ICDD standards. The ICDD file revealed that all of the xonotlite completely turned into wollastonite.

3.2.3. Mechanical Analysis

The cold crushing strengths (CCS) of the porous wollastonite monoliths were determined as a procedure explained in **Chapter 2.3.3** for each composition which gave in **Table 2.2**. In each set of each group, **Equation 2.2** given in **Chapter 2.3.3** was used to calculate the CCS (in kPa). Besides that, the porosity of each monolith part calculated by using **Equation 1.2**. **Figures 3.9-3.21** show compressive strength-strain curves of the porous samples while **Tables 3.1-3.12** show results of the CCS test and measured porosity of each sample of each set.

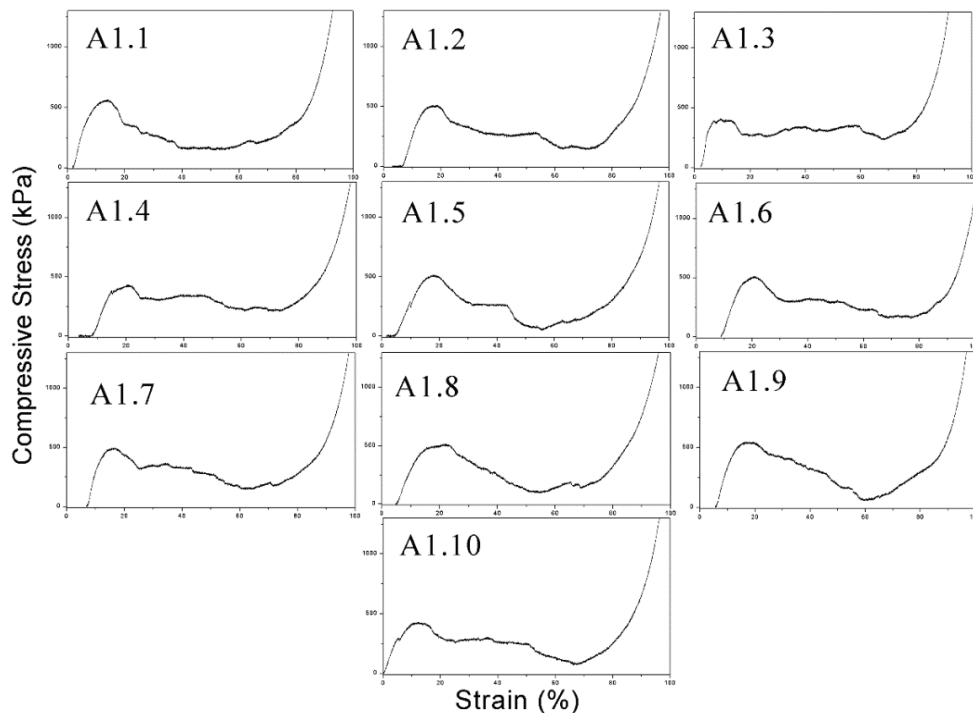


Figure 3.9. The compressive strength- strain diagrams of set A1 samples.

Table 3.1 Results of the set A1

Sample code	Measured porosity (vol%)	Compressive Strength (kPa)
A1.1	88.31	557.20
A1.2	90.11	504.80
A1.3	90.44	404.00
A1.4	90.36	426.40
A1.5	89.33	508.10
A1.6	89.42	505.70
A1.7	89.58	490.60
A1.8	89.26	509.90
A1.9	89.02	537.00
A1.10	90.24	426.00
Mean with Std	89.61 ± 0.68	486.97 ± 50.93

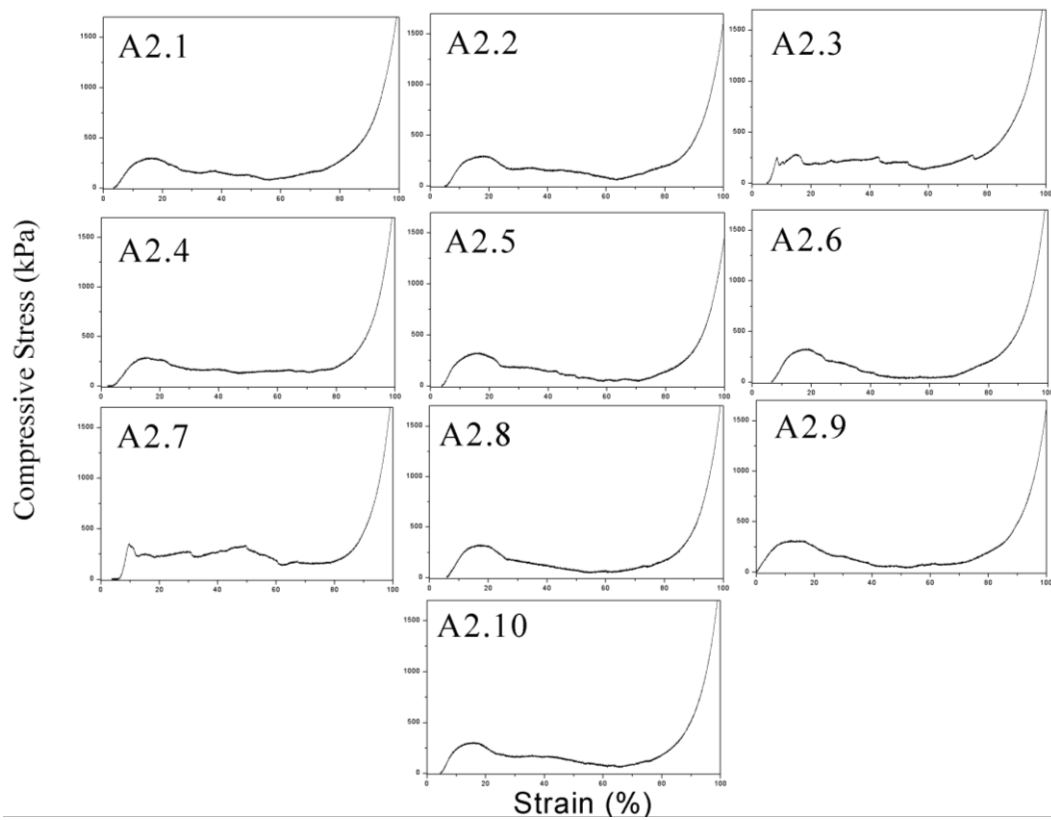


Figure 3.10. The compressive strength- strain diagrams of set A2 samples.

Table 3.2 Results of the set A2

Sample code	Measured porosity (vol%)	Compressive Strength (kPa)
A2.1	91.22	300.19
A2.2	91.23	296.64
A2.3	91.29	285.14
A2.4	91.29	287.20
A2.5	91.05	323.18
A2.6	91.06	326.13
A2.7	90.91	350.48
A2.8	91.17	322.55
A2.9	91.21	308.19
A2.10	91.25	299.58
Mean with Std	91.17 ± 0.12	309.93 ± 20.42

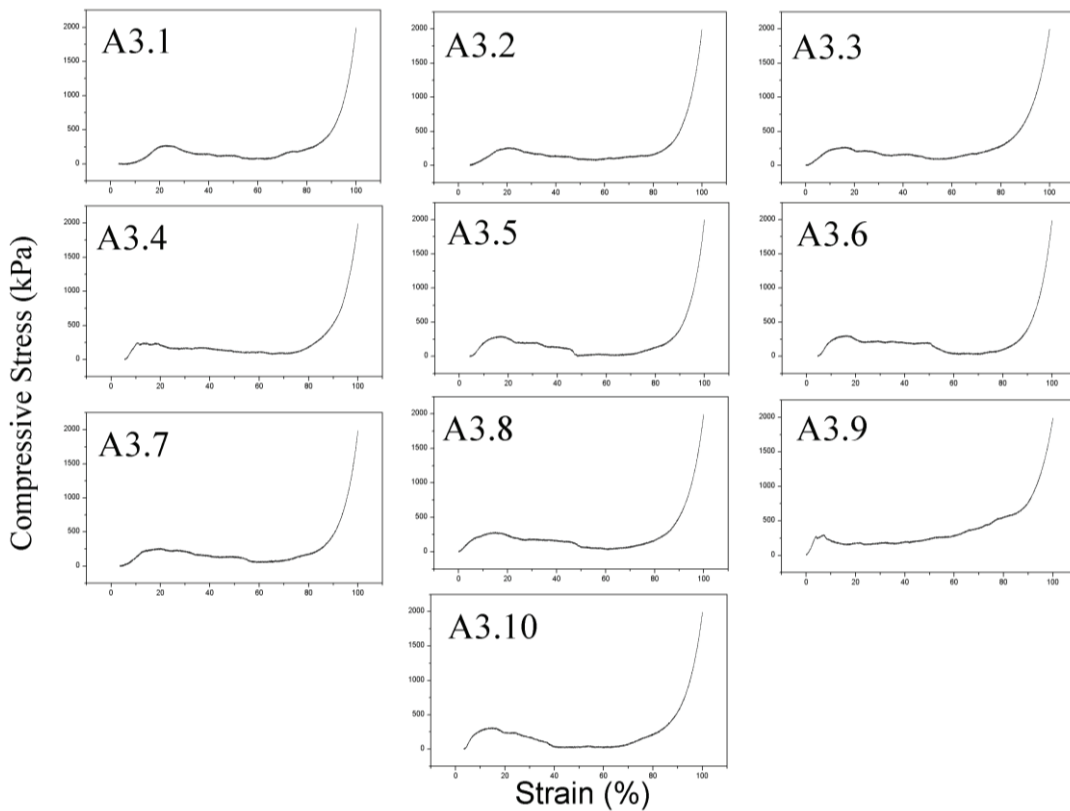


Figure 3.11. The compressive strength- strain diagrams of set A3 samples.

Table 3.3 Results of the set A3

Sample code	Measured porosity (vol%)	Compressive Strength (kPa)
A3.1	91.43	273.95
A3.2	91.47	262.11
A3.3	91.29	272.08
A3.4	91.66	241.00
A3.5	91.28	290.63
A3.6	91.18	300.02
A3.7	91.59	255.26
A3.8	91.24	283.72
A3.9	91.19	292.66
A3.10	91.14	309.10
Mean with Std	91.35 ± 0.18	278.05 ± 21.21

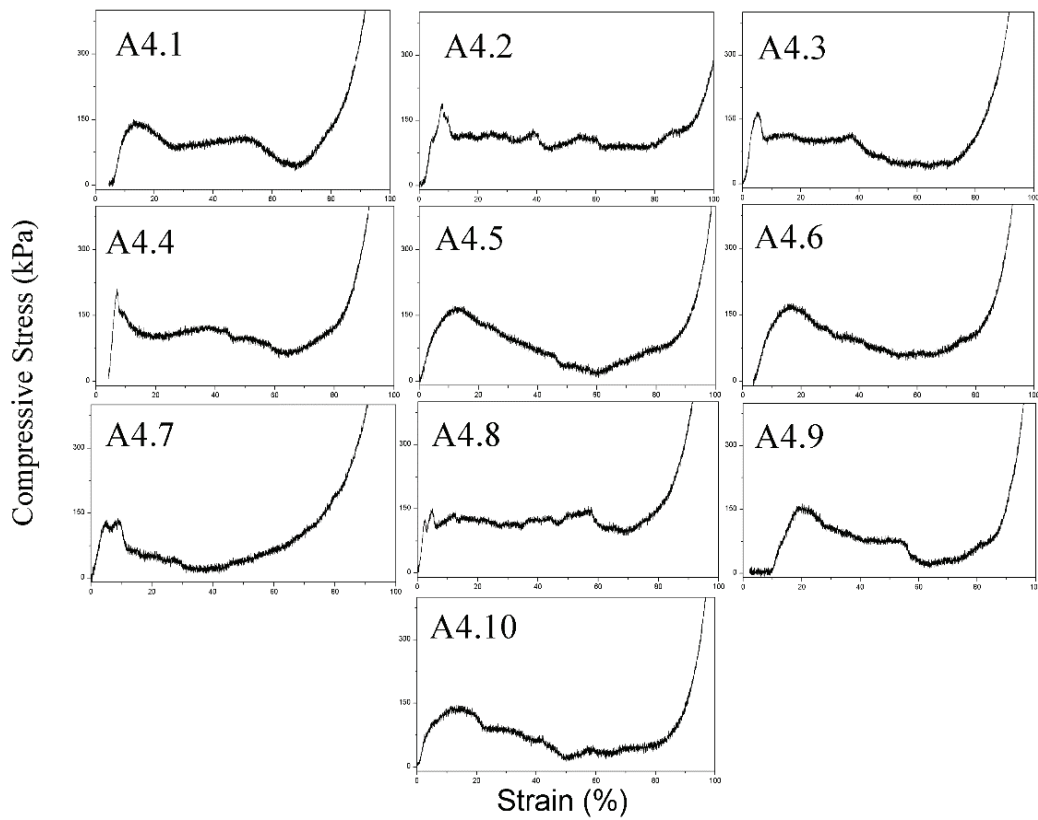


Figure 3.12. The compressive strength- strain diagrams of set A4 samples.

Table 3.4 Results of the set A4

Sample code	Measured porosity (vol%)	Compressive Strength (kPa)
A4.1	92.58	142.43
A4.2	92.27	186.63
A4.3	92.44	162.44
A4.4	92.13	203.84
A4.5	92.46	166.82
A4.6	92.42	170.38
A4.7	92.63	132.60
A4.8	92.59	142.71
A4.9	92.25	185.16
A4.10	92.62	138.21
Mean with Std	92.43 ± 0.17	163.21 ± 23.94

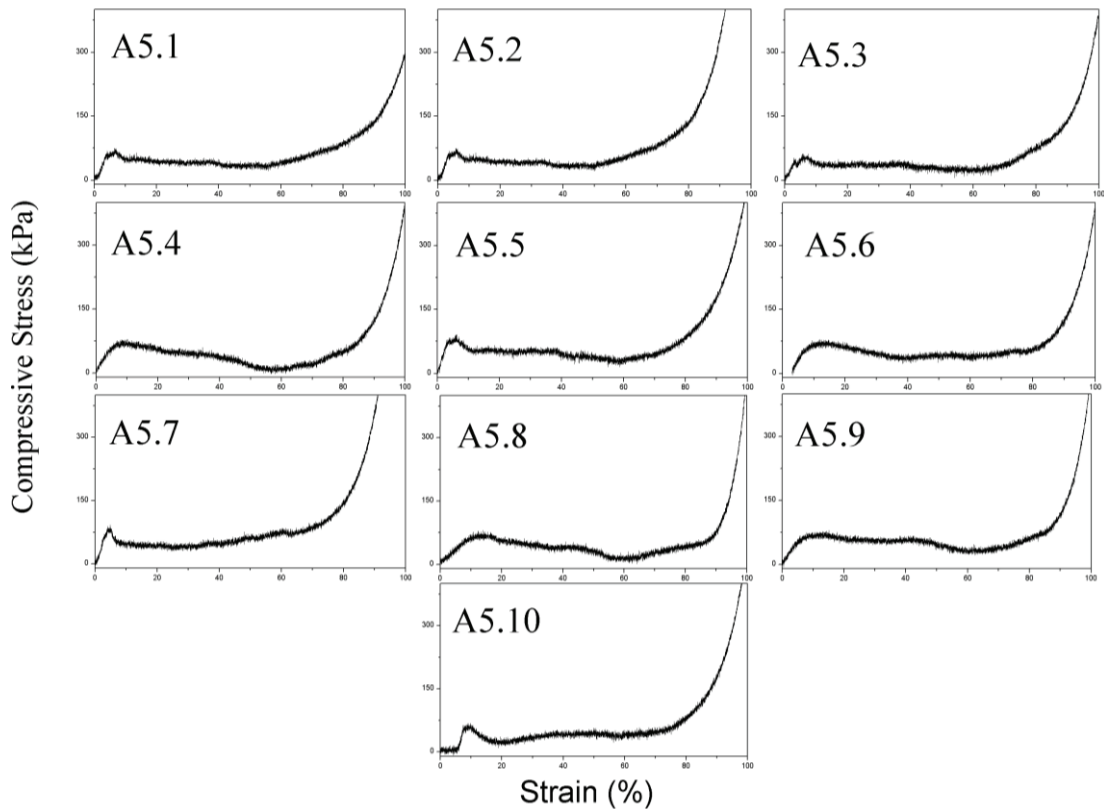


Figure 3.13. The compressive strength- strain diagrams of set A5 samples.

Table 3.5 Results of the set A5

Sample code	Measured porosity (vol%)	Compressive Strength (kPa)
A5.1	93.42	66.46
A5.2	93.41	68.55
A5.3	93.54	53.18
A5.4	93.30	73.30
A5.5	93.24	83.82
A5.6	93.36	73.09
A5.7	93.28	83.00
A5.8	93.38	70.15
A5.9	93.33	73.31
A5.10	93.45	62.78
Mean with Std	93.38 ± 0.12	70.76 ± 9.04

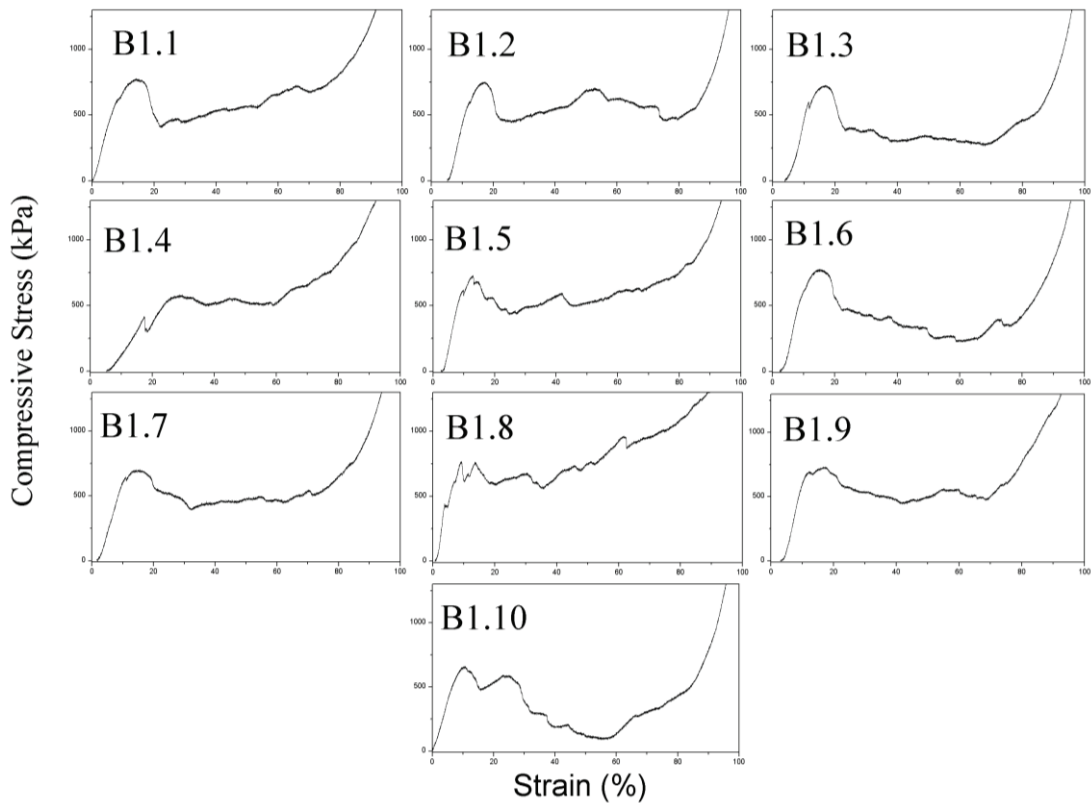


Figure 3.14. The compressive strength- strain diagrams of set B1 samples.

Table 3.6 Results of the set B1

Sample code	Measured porosity (vol%)	Compressive Strength (kPa)
B1.1	88.45	774.43
B1.2	88.73	747.99
B1.3	89.01	715.63
B1.4	89.10	568.59
B1.5	88.75	718.29
B1.6	88.48	774.58
B1.7	88.95	695.30
B1.8	88.53	765.39
B1.9	88.71	724.00
B1.10	88.98	686.89
Mean with Std	88.77 ± 0.23	717.11 ± 60.89

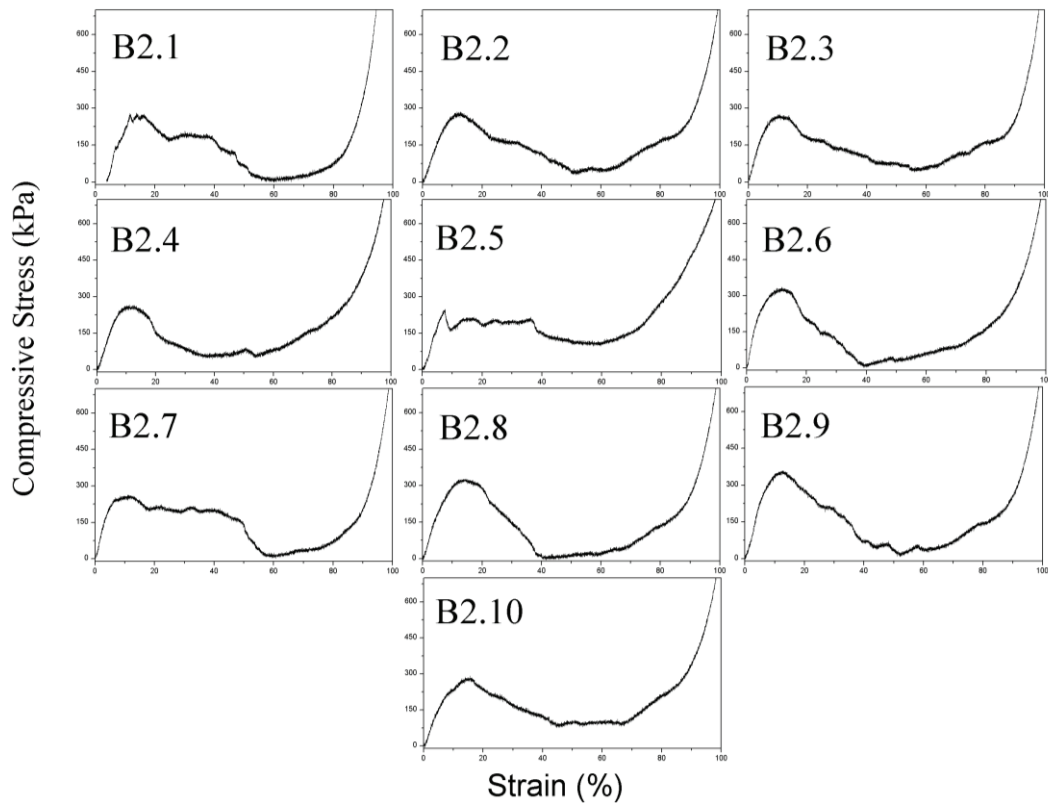


Figure 3.15. The compressive strength- strain diagrams of set B2 samples.

Table 3.7 Results of the set B2

Sample code	Measured porosity (vol%)	Compressive Strength (kPa)
B2.1	91.29	279.66
B2.2	91.23	279.11
B2.3	91.26	272.01
B2.4	91.27	267.43
B2.5	91.44	248.99
B2.6	91.08	325.76
B2.7	91.40	255.39
B2.8	91.02	323.18
B2.9	90.87	348.41
B2.10	91.33	278.53
Mean with Std	91.22 ± 0.18	287.85 ± 33.02

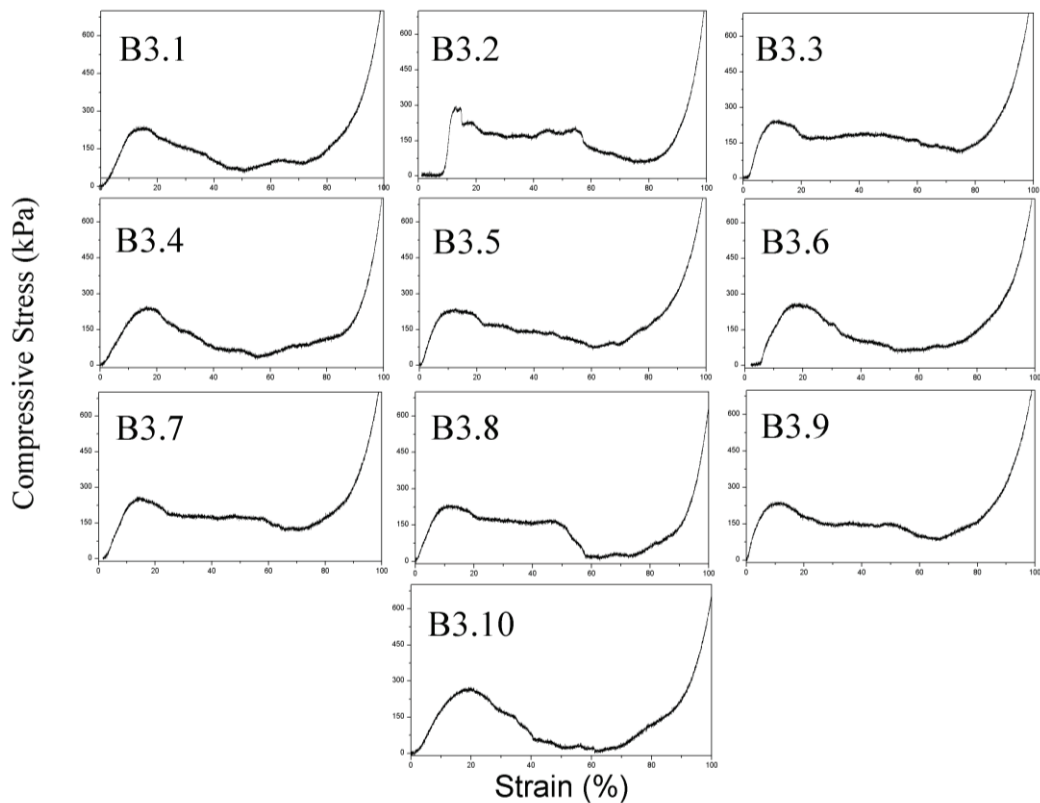


Figure 3.16. The compressive strength- strain diagrams of set B3 samples.

Table 3.8 Results of the set B3

Sample code	Measured porosity (vol%)	Compressive Strength (kPa)
B3.1	91.60	237.58
B3.2	91.09	291.24
B3.3	91.48	246.79
B3.4	91.51	242.57
B3.5	91.57	235.74
B3.6	91.42	254.12
B3.7	91.18	261.08
B3.8	91.42	232.90
B3.9	91.57	237.39
B3.10	91.26	269.58
Mean with Std	91.41 ± 0.18	250.90 ± 18.53

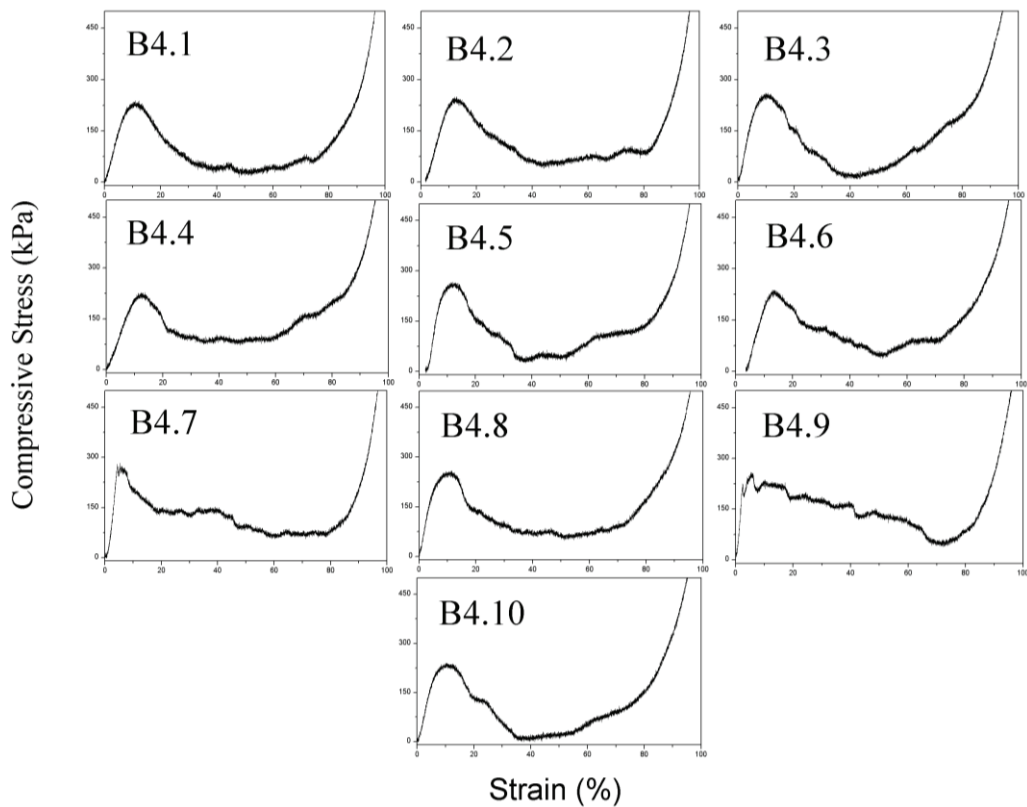


Figure 3.17. The compressive strength- strain diagrams of set B4 samples.

Table 3.9 Results of the set B4

Sample code	Measured porosity (vol%)	Compressive Strength (kPa)
B4.1	91.90	225.69
B4.2	91.49	242.43
B4.3	91.42	248.25
B4.4	91.88	221.33
B4.5	91.25	247.56
B4.6	91.77	230.01
B4.7	91.27	252.62
B4.8	91.63	236.44
B4.9	91.19	242.91
B4.10	91.72	224.36
Mean with Std	91.55 ± 0.27	237.16 ± 11.20

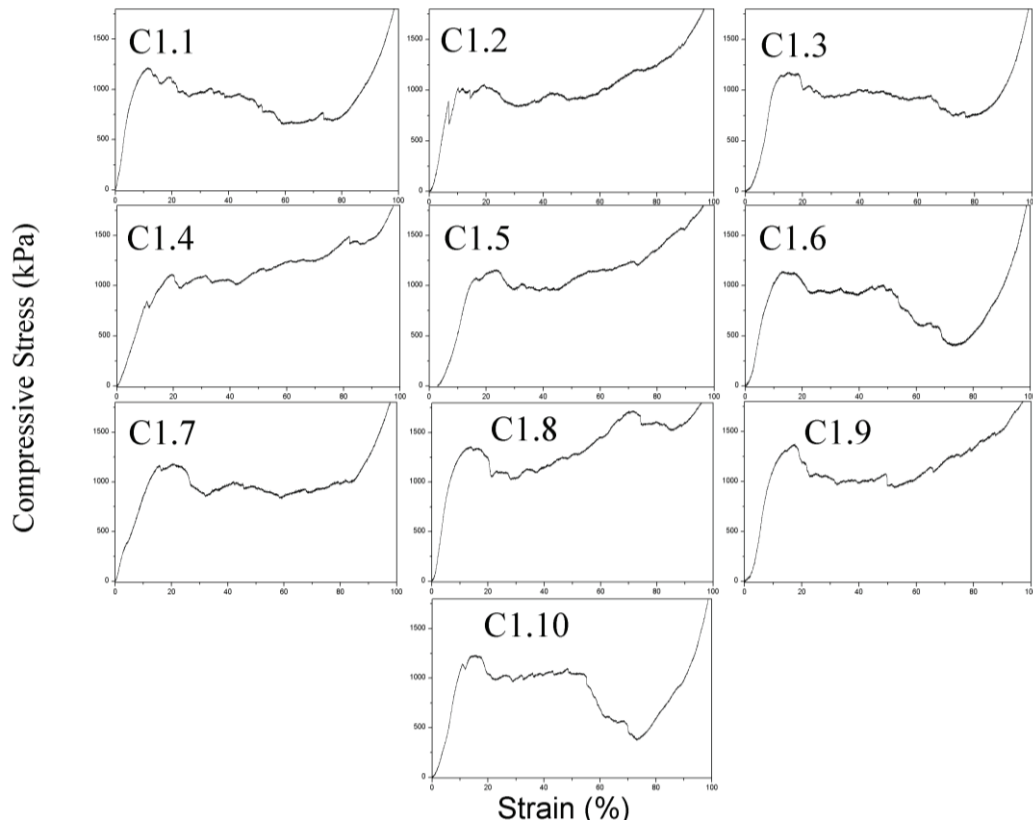


Figure 3.18. The compressive strength- strain diagrams of set C1 samples.

Table 3.10 Results of the set C1

Sample code	Measured porosity (vol%)	Compressive Strength (kPa)
C1.1	87.58	1218.16
C1.2	88.40	900.85
C1.3	87.78	1179.28
C1.4	87.89	1103.36
C1.5	88.07	1160.81
C1.6	88.16	1144.52
C1.7	87.61	1164.99
C1.8	87.32	1361.63
C1.9	87.39	1376.04
C1.10	88.03	1229.03
Mean with Std	87.82 ± 0.35	1183.87 ± 133.66

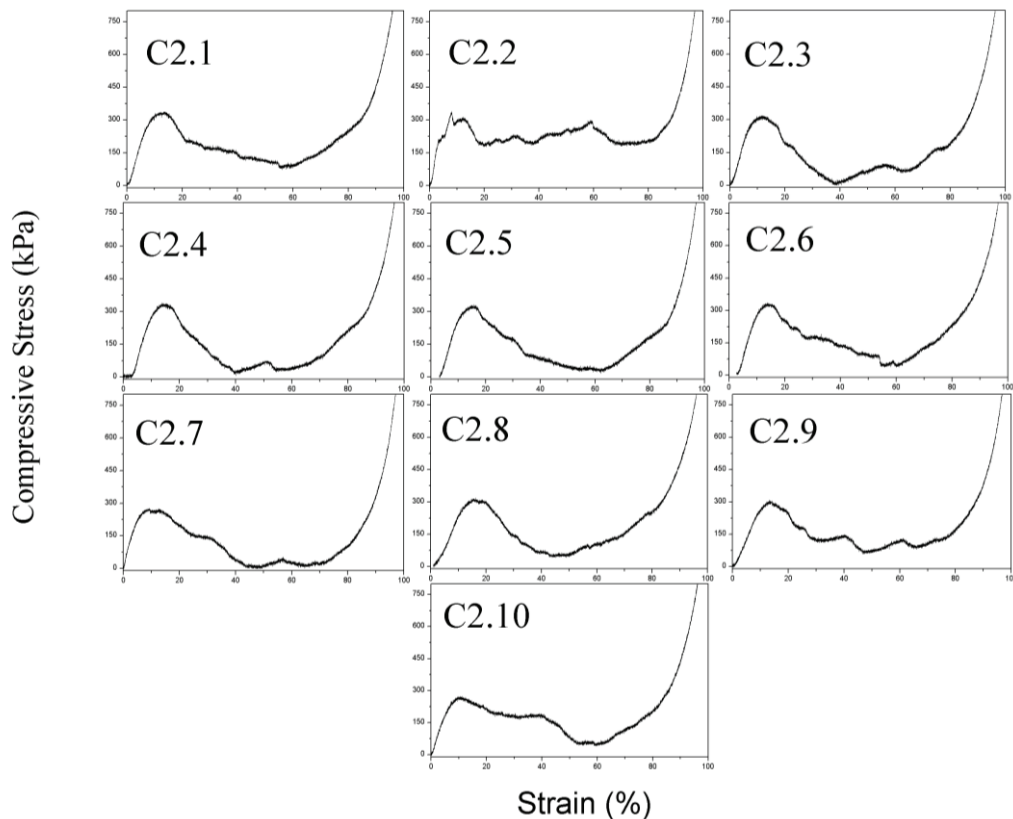


Figure 3.19. The compressive strength- strain diagrams of set C2 samples.

Table 3.11 Results of the set C2

Sample code	Measured porosity (vol%)	Compressive Strength (kPa)
C2.1	90.29	332.72
C2.2	90.17	338.09
C2.3	90.42	316.13
C2.4	90.42	335.96
C2.5	90.20	326.49
C2.6	90.28	325.43
C2.7	90.56	290.63
C2.8	90.31	307.28
C2.9	90.54	308.77
C2.10	90.68	270.72
Mean with Std	90.39 ± 0.17	315.22 ± 21.55

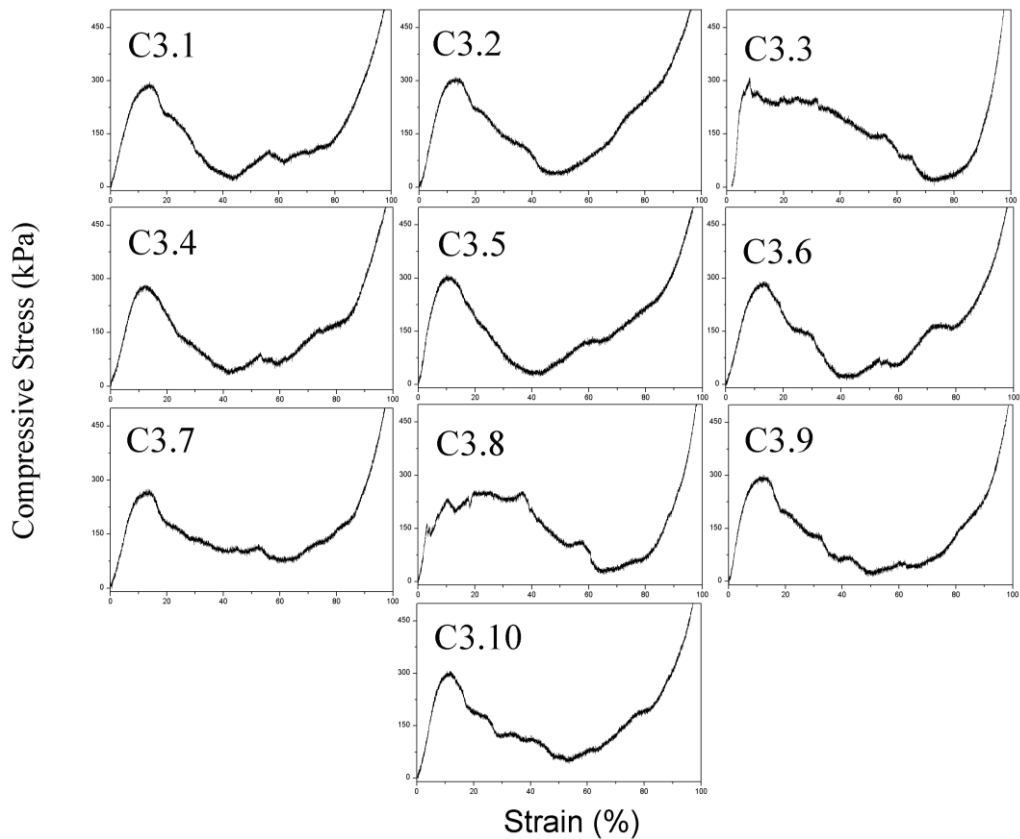


Figure 3.20. The compressive strength- strain diagrams of set C3 samples.

Table 3.12 Results of the set C3

Sample code	Measured porosity (vol%)	Compressive Strength (kPa)
C3.1	90.61	291.92
C3.2	90.86	304.58
C3.3	90.70	291.76
C3.4	90.76	280.70
C3.5	90.97	296.50
C3.6	90.62	283.09
C3.7	90.99	274.83
C3.8	91.12	252.78
C3.9	90.47	298.15
C3.10	90.51	299.16
Mean with Std	90.76 ± 0.22	287.35 ± 15.24

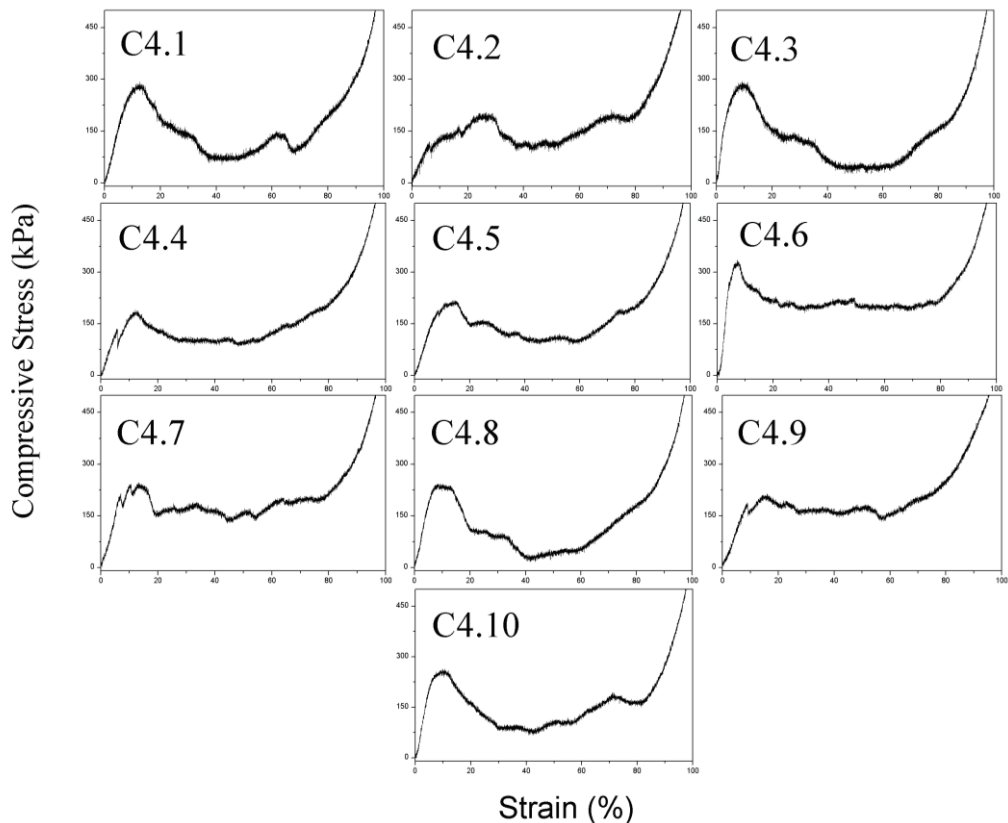


Figure 3.21. The compressive strength- strain diagrams of set C4 samples.

Table 3.13 Results of the set C4

Sample code	Measured porosity (vol%)	Compressive Strength (kPa)
C4.1	91.73	174.59
C4.2	92.06	194.38
C4.3	92.11	144.58
C4.4	91.82	172.54
C4.5	91.68	214.41
C4.6	90.90	314.12
C4.7	91.29	231.87
C4.8	91.07	235.65
C4.9	91.44	194.71
C4.10	91.33	259.27
Mean with Std	91.54 ± 0.41	213.61 ± 49.11

The cold crushing strength curves of the porous wollastonite had similarities with stress-strain curves of the brittle foams which were mentioned in **Chapter 1.1.2**. These similarities were yield point, peaks in plateau region and densification region. Peaks occurred after the yield point, and these peaks in the probably resulted from the brittle nature of the porous structure.⁸⁰ **Figures 3.22-24** showed the relationship between porosity and compressive strength of porous monoliths.

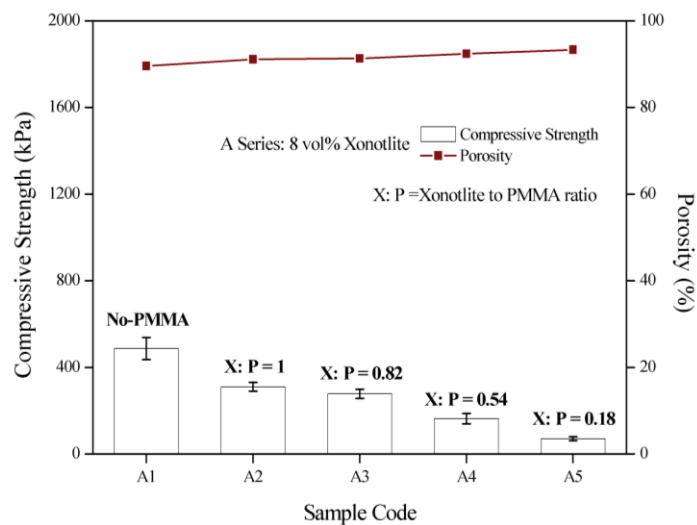


Figure 3.22. Illustration of the compressive strength and porosity of the A series.

In literature, many researchers studied the relationship between the porosity and compressive strength behavior of porous ceramics.^{55, 81} All these studies showed that there is a relationship which depends on pore characteristics such as pore shape, size, and distribution. In the present study, for determination of the effect of the amount of porogen, other porogen characteristics such as pore shape and size was kept constant.

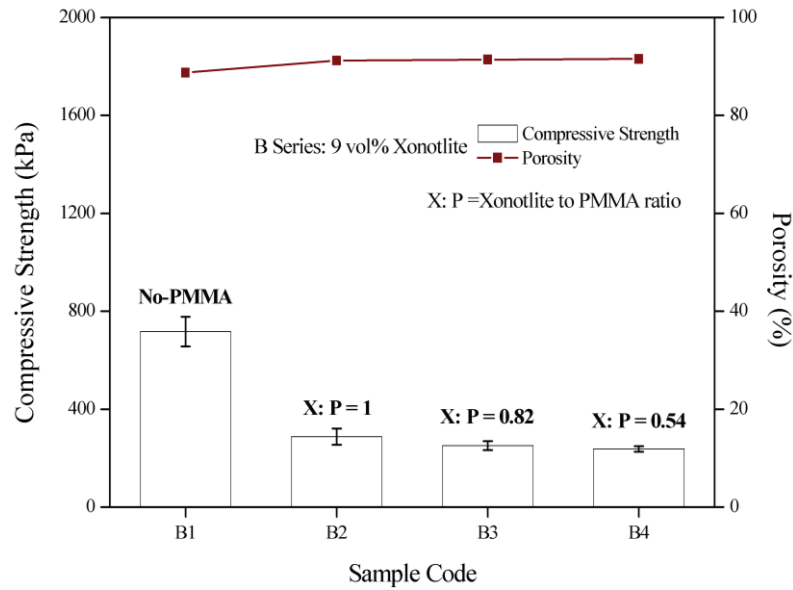


Figure 3.23. Illustration of the compressive strength and porosity of the B series.

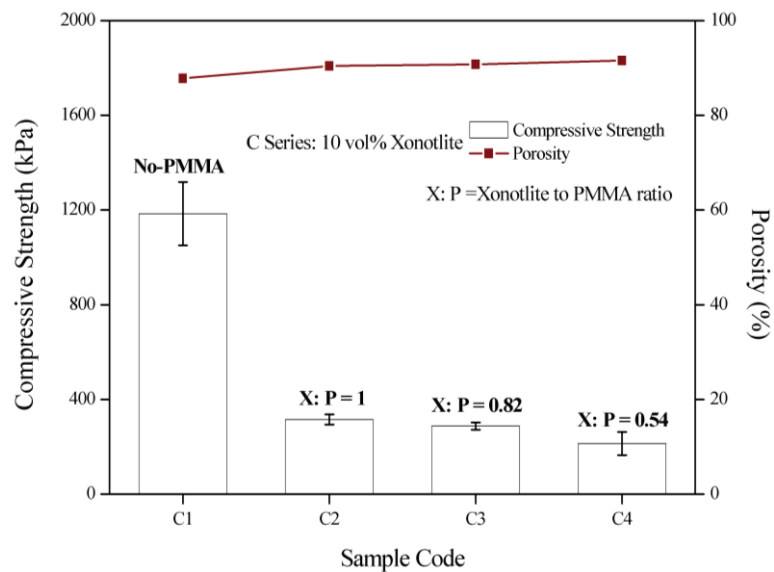


Figure 3.24. Illustration of the compressive strength and porosity of the C series.

As far as cold crushing strength was concerned, it noticed that the presence (i.e. A2, B2, and C2) and absence (i.e. A1, B1, and C1) of the PMMA created dramatic differences in compressive strength. The compressive strength of the A1, B1, and C1 monoliths were much higher than A2, B2, and C2 porous monoliths. In no PMMA samples, needle-like wollastonite particles interlocked under compressive stress so enhanced strength. On the other side, when the PMMA volume increased, the strength value reduced due to only solid parts between cell structures carried the compressive stress. Monoliths with a xonotlite-to-PMMA ratio of 1 (i.e. A2, B2, and C2) appeared to have higher cold crushing strength than monoliths with 0.82 (i.e. A3, B3, and C3), 0.54 (i.e. A4, B4, and C4), and 0.18 (i.e. A5) xonotlite-to-PMMA ratios. It can be concluded that the increase in the amount of PMMA, which means increasing the porosity, influenced the porosity-compressive strength relationship of porous monolith parts for the results. In general, increasing amount of the matrix material improves package density and provides lower porosity but porosity of B2 and B3 samples (consist of 9% vol. xonotlite) was slightly higher than A2 and A3 samples (consists of 8% vol. xonotlite). Therefore, the average compressive strength of B2 and B3 was lower than A2 and A3. On the other hand, **Figure 3.22-24** and **Figure 3.25** shows that when the keeping xonotlite amount increased and the xonotlite to PMMA ratio remained constant, the compressive strength of the porous monoliths increased.

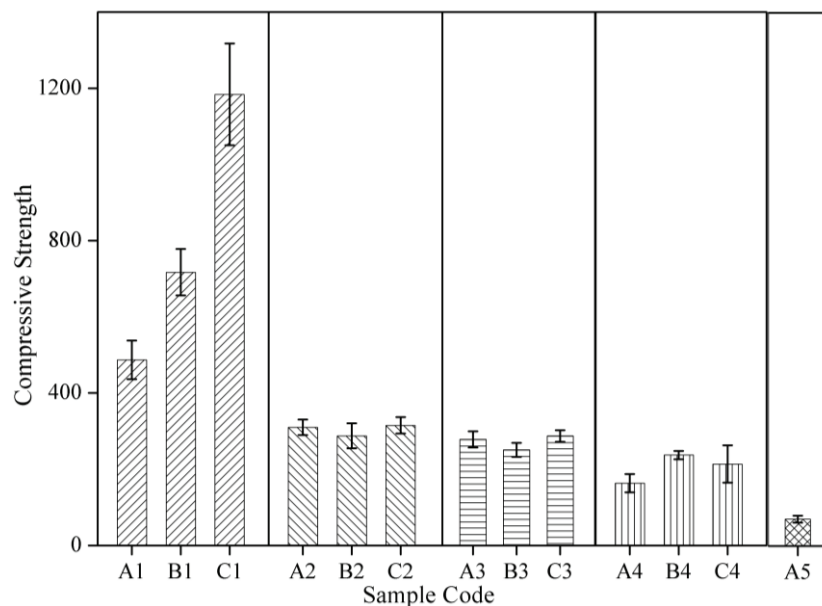


Figure 3.25. Comparison of the Cold Crushing Strength of each set.

CHAPTER 4

CONCLUSIONS

In the present thesis, the feasibility of the porous wollastonite monolith parts as an Aircraft Arresting Material (AAS) was investigated. The needle-like xonotlite particles and the PMMA microbeads were used as matrix phase and sacrificial templating agent, respectively. Slip casting technique was used to form monolith parts.

When the results of the present study compared with similar studies published earlier, the porous wollastonite parts developed as the AAS in this work were possessed advantages such as compressive strength and high-temperature durability. The results of this work suggested that porous wollastonite parts with desired the AAS conditions could be designed by controlling the xonotlite to PMMA ratio and the xonotlite amount. The mechanical strength and porosity of the porous monolith parts were affected by the amount of the porosity. The compressive strength and porosity of the porous monoliths were in between 53.18 kPa and 1376.04 kPa and 87.32 and 93.54, respectively, by regulating the xonotlite to PMMA ratio and the amount of xonotlite. The porous wollastonite monoliths coded as A4, B4, and C4 demonstrated ideal compressive strength and porosity conditions required to be used as the AAS.

Future studies may be directed towards reducing carbon footprint by using another porogen instead of the PMMA or another production or forming method may be considered. This can be accomplished by alteration the pore-forming agent, the manufacturing method of porous monoliths.

REFERENCES

1. Bee on a honeycomb. <https://www.britannica.com/science/honeycomb-biology/media/270928/125876> (accessed February 17, 2019).
2. Lee, D., *Biomimicry: Inventions Inspired by Nature*. Kids Can Press Ltd: 2011.
3. Colombo, P.; Vakifahmetoglu, C.; Costacurta, S., Fabrication of ceramic components with hierarchical porosity. *Journal of materials science* 2010, 45 (20), 5425-5455.
4. Gibson, L. J.; Ashby, M. F., *Cellular solids: structure and properties*. Cambridge university press: 1999.
5. Zhang, M.; Li, J., Carbon nanotube in different shapes. *Materials today* 2009, 12 (6), 12-18.
6. Greil, P.; Lifka, T.; Kaindl, A., Biomorphic cellular silicon carbide ceramics from wood: II. Mechanical properties. *Journal of the European Ceramic Society* 1998, 18 (14), 1975-1983.
7. Green, D. J.; Colombo, P., Cellular ceramics: intriguing structures, novel properties, and innovative applications. *MRS bulletin* 2003, 28 (4), 296-300.
8. Colombo, P., In praise of pores. *Science* 2008, 322 (5900), 381-383.
9. Colombo, P., Conventional and novel processing methods for cellular ceramics. *Philosophical Transactions of the Royal Society A: Mathematical, Physical and Engineering Sciences* 2005, 364 (1838), 109-124.
10. Gibson, L., Modelling the mechanical behavior of cellular materials. *Materials Science and Engineering: A* 1989, 110, 1-36.
11. Lucas, P. A., Coffee cup and container. Google Patents: 1979.
12. Yatağanbaba, A.; Kurtbaş, İ., Effect of heating position on thermal energy storage in cavity with/without open-cell metallic foams. *Experimental Heat Transfer* 2016, 29 (3), 355-377.
13. Bastawros, A.; Bart-Smith, H.; Evans, A., Experimental analysis of deformation mechanisms in a closed-cell aluminum alloy foam. *Journal of the Mechanics and Physics of Solids* 2000, 48 (2), 301-322.
14. Askeland, D. R.; Phule, P. P., *The science and engineering of materials*. Springer: 2003.

15. Colombo, P.; Hellmann, J. R.; Shelleman, D. L., Thermal shock behavior of silicon oxycarbide foams. *Journal of the American Ceramic Society* 2002, 85 (9), 2306-2312.
16. Ashby, M., The properties of foams and lattices. *Philosophical Transactions of the Royal Society A: Mathematical, Physical and Engineering Sciences* 2005, 364 (1838), 15-30.
17. Ashby, M. F.; Medalist, R. M., The mechanical properties of cellular solids. *Metallurgical Transactions A* 1983, 14 (9), 1755-1769.
18. Scheffler, M.; Colombo, P., *Cellular ceramics: structure, manufacturing, properties and applications*. John Wiley & Sons: 2006.
19. Vakifahmetoglu, C., Fabrication and properties of ceramic 1D nanostructures from preceramic polymers: a review. *Advances in Applied Ceramics* 2011, 110 (4), 188-204.
20. Studart, A. R.; Gonzenbach, U. T.; Tervoort, E.; Gauckler, L. J., Processing routes to macroporous ceramics: a review. *Journal of the American Ceramic Society* 2006, 89 (6), 1771-1789.
21. Taslicukur, Z.; Balaban, C.; Kuskonmaz, N., Production of ceramic foam filters for molten metal filtration using expanded polystyrene. *Journal of the European Ceramic Society* 2007, 27 (2-3), 637-640.
22. Hammel, E.; Ighodaro, O.-R.; Okoli, O., Processing and properties of advanced porous ceramics: An application based review. *Ceramics International* 2014, 40 (10), 15351-15370.
23. Karl, S.; Somers, A. V., Method of making porous ceramic articles. Google Patents: 1963.
24. Voorhees, P. W., The theory of Ostwald ripening. *Journal of Statistical Physics* 1985, 38 (1-2), 231-252.
25. Svanholm, G., Process and plant for manufacture of aerated concrete. Google Patents: 1990.
26. Narayanan, N.; Ramamurthy, K., Structure and properties of aerated concrete: a review. *Cement and Concrete composites* 2000, 22 (5), 321-329.
27. Kurama, H.; Topcu, I.; Karakurt, C., Properties of the autoclaved aerated concrete produced from coal bottom ash. *Journal of materials processing technology* 2009, 209 (2), 767-773.
28. Colombo, P.; Hellmann, J. R.; Shelleman, D. L., Mechanical properties of silicon oxycarbide ceramic foams. *Journal of the American Ceramic Society* 2001, 84 (10), 2245-2251.

29. Colombo, P.; Gambaryan-Roisman, T.; Scheffler, M.; Buhler, P.; Greil, P., Conductive ceramic foams from preceramic polymers. *Journal of the American Ceramic Society* 2001, 84 (10), 2265-2268.
30. Colombo, P.; Bernardo, E.; Biasetto, L., Novel microcellular ceramics from a silicone resin. *Journal of the American Ceramic Society* 2004, 87 (1), 152-154.
31. Twigg, M. V.; Richardson, J. T., Fundamentals and applications of structured ceramic foam catalysts. *Industrial & engineering chemistry research* 2007, 46 (12), 4166-4177.
32. Tiller, F. M.; Tsai, C. D., Theory of filtration of ceramics: I, slip casting. *Journal of the American Ceramic Society* 1986, 69 (12), 882-887.
33. Wang, F. F., *Ceramic fabrication processes: Treatise on materials science and technology*. Elsevier: 2016; Vol. 9.
34. Rahaman, M. N., *Ceramic processing and sintering*. CRC press: 2003.
35. Le Ferrand, H.; Bouville, F.; Niebel, T. P.; Studart, A. R., Magnetically assisted slip casting of bioinspired heterogeneous composites. *Nature materials* 2015, 14 (11), 1172.
36. Yu, J.; Yang, J.; Huang, Y., The transformation mechanism from suspension to green body and the development of colloidal forming. *Ceramics International* 2011, 37 (5), 1435-1451.
37. Richardson, I., The calcium silicate hydrates. *Cement and concrete research* 2008, 38 (2), 137-158.
38. Hansen, M. R.; Jakobsen, H. J.; Skibsted, J., ²⁹Si chemical shift anisotropies in calcium silicates from high-field ²⁹Si MAS NMR spectroscopy. *Inorganic chemistry* 2003, 42 (7), 2368-2377.
39. Black, L.; Garbev, K.; Stemmermann, P.; Hallam, K. R.; Allen, G. C., *X-ray Photoelectron Spectroscopy (XPS): A New Means of Studying CSH Structure and Chemistry*.
40. Chen, J. J.; Thomas, J. J.; Taylor, H. F.; Jennings, H. M., Solubility and structure of calcium silicate hydrate. *Cement and concrete research* 2004, 34 (9), 1499-1519.
41. Shaw, S.; Clark, S.; Henderson, C., Hydrothermal formation of the calcium silicate hydrates, tobermorite (Ca₅Si₆O₁₆(OH)₂·4H₂O) and xonotlite (Ca₆Si₆O₁₇(OH)₂): an in situ synchrotron study. *Chemical Geology* 2000, 167 (1-2), 129-140.
42. Cao, J.; Liu, F.; Lin, Q.; Zhang, Y., Hydrothermal synthesis of xonotlite from carbide slag. *Progress in Natural Science* 2008, 18 (9), 1147-1153.

43. Yanagisawa, K.; Feng, Q.; Yamasaki, N., Hydrothermal synthesis of xonotlite whiskers by ion diffusion. *Journal of materials science letters* 1997, 16 (11), 889-891.
44. Milestone, N.; Ahari, G. K., Hydrothermal processing of xonotlite based compositions. *Advances in Applied ceramics* 2007, 106 (6), 302-308.
45. Black, L.; Garbev, K.; Stumm, A., Structure, bonding and morphology of hydrothermally synthesised xonotlite. *Advances in Applied Ceramics* 2009, 108 (3), 137-144.
46. Vukovich Jr, M., Effect of wollastonite substitutions in a semivitreous dinnerware body. *Journal of the American Ceramic Society* 1956, 39 (10), 323-329.
47. De Aza, P.; Luklinska, Z.; Anseau, M.; Hector, M.; Guitian, F.; De Aza, S., Reactivity of a wollastonite–tricalcium phosphate Bioeutectic® ceramic in human parotid saliva. *Biomaterials* 2000, 21 (17), 1735-1741.
48. Li, X.; Chang, J., Synthesis of wollastonite single crystal nanowires by a novel hydrothermal route. *Chemistry letters* 2004, 33 (11), 1458-1459.
49. Risbud, M.; Saheb, D. N.; Jog, J.; Bhonde, R., Preparation, characterization and in vitro biocompatibility evaluation of poly (butylene terephthalate)/wollastonite composites. *Biomaterials* 2001, 22 (12), 1591-1597.
50. Meng, M.-R.; Dou, Q., Effect of pimelic acid on the crystallization, morphology and mechanical properties of polypropylene/wollastonite composites. *Materials Science and Engineering: A* 2008, 492 (1-2), 177-184.
51. Wu, J.; Zhu, Y.-J.; Cheng, G.-F.; Huang, Y.-H., Microwave-assisted preparation of $\text{Ca}_6\text{Si}_6\text{O}_{17}(\text{OH})_2$ and $\beta\text{-CaSiO}_3$ nanobelts. *Materials Research Bulletin* 2010, 45 (4), 509-512.
52. Dent, L.; Taylor, H., The dehydration of xonotlite. *Acta Crystallographica* 1956, 9 (12), 1002-1004.
53. Vakifahmetoglu, C., Zeolite decorated highly porous acicular calcium silicate ceramics. *Ceramics International* 2014, 40 (8), 11925-11932.
54. Xie, J.; Shao, H.; He, D.; Yang, X.; Yao, C.; Ye, J.; He, Y.; Fu, J.; Gou, Z., Ultrahigh strength of three-dimensional printed diluted magnesium doping wollastonite porous scaffolds. *MRS Communications* 2015, 5 (4), 631-639.
55. Lin, K.; Chang, J.; Zeng, Y.; Qian, W., Preparation of macroporous calcium silicate ceramics. *Materials Letters* 2004, 58 (15), 2109-2113.
56. Heymsfield, E.; Hale, W. M.; Halsey, T. L., Aircraft response in an airfield arrestor system during an overrun. *Journal of transportation engineering* 2012, 138 (3), 284-292.

57. David, R. E. Location of commercial aircraft accidents/incidents relative to runways; Federal Aviation Administration Washington DC: 1990.
58. Heymsfield, E.; Marisetty, S. C., Performance prediction of the strong company's soft ground arrestor system using a numerical analysis. Mack-Blackwell National Rural Transportation Center, University of Arkansas: 2009.
59. Heymsfield, E., Predicting aircraft stopping distances within an EMAS. *Journal of Transportation Engineering* 2013, 139 (12), 1184-1193.
60. Kirkland, I.; Caves, R., New aircraft overrun database, 1980-1998. *Transportation Research Record: Journal of the Transportation Research Board* 2002, (1788), 93-100.
61. Cook, R. Soft-Ground Arresting System for Commercial Aircraft; DOT/FAA/CT-TN93/4; 1993.
62. Ho, C.-H.; Romero, P. In Investigation of existing engineered material arresting system at three US Airports, *Proceedings of 50th Annual Forum of Transportation Research Forum*, Portland, Oregon, USA, 2009.
63. Legatski, L. A. In *Structural considerations of cellular concrete, Materials and Member Behavior*, ASCE: 1987; pp 435-441.
64. Schober, G. In Effect of size distribution of air pores in AAC on compressive strength, *Proceedings of the 3rd Rilem International Symposium on Autoclaved Aerated Concrete*, Zürich, Switzerland, 1992; pp 77-80.
65. Heymsfield, E.; Halsey, T., Sensitivity analysis of engineered material arrestor systems to aircraft and arrestor material characteristics. *Transportation Research Record: Journal of the Transportation Research Board* 2008, (2052), 110-117.
66. Bassani, M.; Sacchi, E.; Canonico, F., Performance prediction for innovative crushable material used in aircraft arrestor beds. *Journal of Materials in Civil Engineering* 2011, 24 (6), 725-734.
67. Kearsley, E.; Wainwright, P., The effect of high fly ash content on the compressive strength of foamed concrete. *Cement and concrete research* 2001, 31 (1), 105-112.
68. Han, B.; Zhang, L.; Ou, J., *Smart and Multifunctional Concrete Towards Sustainable Infrastructures*. Springer: 2017.
69. Heymsfield, E.; Hale, W. M.; Halsey, T., A parametric sensitivity analysis of soft ground arrestor systems. In *Aviation: A World of Growth*, 2007; pp 227-236.
70. Barsotti, M. A.; Puryear, J. M. H.; Stevens, D. J., Developing improved civil aircraft arresting systems. *Transportation Research Board*: 2009; Vol. 29.
71. Santagata, E.; Bassani, M.; Sacchi, E., Performance of new materials for aircraft arrestor beds. *Transportation Research Record: Journal of the Transportation Research Board* 2010, (2177), 124-131.

72. Marisetty, S. C.; Bailey, E. D.; Hale, W. M.; Heymsfield, E. P., Development of a soft ground arrestor system. US Dept. of Transportation, Fayetteville, AR 2008.
73. Heymsfield, E.; Hale, W. M.; Halsey, T. L., Optimizing low density concrete behavior for soft ground arrestor systems. In *Airfield and Highway Pavements: Efficient Pavements Supporting Transportation's Future*, 2008; pp 122-133.
74. Zhang, Z.; Yang, J., Improving safety of runway overrun through foamed concrete aircraft arresting system: an experimental study. *International journal of crashworthiness* 2015, 20 (5), 448-463.
75. Zhang, L.; Zhou, D.; Yang, W.; Chen, Y.; Liang, B.; Zhou, J., Preparation of ceramic foams suitable for aircraft arresting by the airport runway based on a protein foaming agent. *Journal of Wuhan University of Technology-Mater. Sci. Ed.* 2014, 29 (5), 980-989.
76. Chen, Y.; Li, Z.; Miao, N., Polymethylmethacrylate (PMMA)/CeO₂ hybrid particles for enhanced chemical mechanical polishing performance. *Tribology International* 2015, 82, 211-217.
77. Panaitescu, D. M.; Frone, A. N.; Ghiurea, M.; Spataru, C. I.; Radovici, C.; Iorga, M. D., Properties of polymer composites with cellulose microfibrils. *Advances in Composite Materials—Ecodesign and Analysis* 2011, 103-122.
78. ASTM, D., 3576, Standard test method for cell size of rigid cellular plastics. *Annual book of ASTM standards* 8.
79. ASTM, C., 773-88, Standard Test Method for Compressive (Crushing) Strength of Fired Whiteware Materials. *Annual Book of ASTM Standards* 2016, 15.02.
80. Fu, Q.; Rahaman, M. N.; Dogan, F.; Bal, B. S., Freeze casting of porous hydroxyapatite scaffolds. II. Sintering, microstructure, and mechanical behavior. *Journal of Biomedical Materials Research Part B: Applied Biomaterials: An Official Journal of The Society for Biomaterials, The Japanese Society for Biomaterials, and The Australian Society for Biomaterials and the Korean Society for Biomaterials* 2008, 86 (2), 514-522.
81. Kearsley, E.; Wainwright, P., The effect of porosity on the strength of foamed concrete. *Cement and concrete research* 2002, 32 (2), 233-239.